nature astronomy

ARTICLES

https://doi.org/10.1038/s41550-020-1174-4

Phosphine gas in the cloud decks of Venus

Jane S. Greaves[1,2]✉, Anita M. S. Richards[3], William Bains[4], Paul B. Rimmer[5,6,7], Hideo Sagawa[8], David L. Clements[9], Sara Seager[4,13,14], Janusz J. Petkowski[4], Clara Sousa-Silva[4], Sukrit Ranjan[4], Emily Drabek-Maunder[1,10], Helen J. Fraser[11], Annabel Cartwright[1], Ingo Mueller-Wodarg[9], Zhuchang Zhan[4], Per Friberg[12], Iain Coulson[12], E'lisa Lee[12] and Jim Hoge[12]

Measurements of trace gases in planetary atmospheres help us explore chemical conditions different to those on Earth. Our nearest neighbour, Venus, has cloud decks that are temperate but hyperacidic. Here we report the apparent presence of phosphine (PH_3) gas in Venus's atmosphere, where any phosphorus should be in oxidized forms. Single-line millimetre-waveband spectral detections (quality up to ~15σ) from the JCMT and ALMA telescopes have no other plausible identification. Atmospheric PH_3 at ~20 ppb abundance is inferred. The presence of PH_3 is unexplained after exhaustive study of steady-state chemistry and photochemical pathways, with no currently known abiotic production routes in Venus's atmosphere, clouds, surface and subsurface, or from lightning, volcanic or meteoritic delivery. PH_3 could originate from unknown photochemistry or geochemistry, or, by analogy with biological production of PH_3 on Earth, from the presence of life. Other PH_3 spectral features should be sought, while in situ cloud and surface sampling could examine sources of this gas.

Studying rocky-planet atmospheres gives clues to how they interact with surfaces and subsurfaces, and whether any non-equilibrium compounds could reflect the presence of life. Characterizing extrasolar-planet atmospheres is extremely challenging, especially for rare compounds[1]. The Solar System thus offers important testbeds for exploring planetary geology, climate and habitability, via both in situ sampling and remote monitoring. Proximity makes signals of trace gases much stronger than those from extrasolar planets, but issues remain in interpretation.

Thus far, Solar System exploration has found compounds of interest, but often in locations where the gas sources are inaccessible, such as the Martian subsurface[2] and water reservoirs inside icy moons[3,4]. Water, simple organics and larger unidentified carbon-bearing species[5–7] are known. However, geochemical sources for carbon compounds may exist[8], and temporal/spatial anomalies can be hard to reconcile, for example, for Martian methane sampled by rovers and observed from orbit[9].

An ideal biosignature gas would be unambiguous. Living organisms should be its sole source, and it should have intrinsically strong, precisely characterized spectral transitions unblended with contaminant lines—criteria that are not usually all achievable. It was recently proposed that any phosphine (PH_3) detected in a rocky planet's atmosphere is a promising sign of life[10]. Trace PH_3 in Earth's atmosphere (parts per trillion abundance globally[11]) is uniquely associated with anthropogenic activity or microbial presence—life produces this highly reducing gas even in an overall oxidizing environment. PH_3 is found elsewhere in the Solar System only in the reducing atmospheres of giant planets[12,13], where it is produced in deep atmospheric layers at high temperatures and pressures, and dredged upwards by convection[14,15]. Solid surfaces of rocky planets present a barrier to their interiors, and PH_3 would be rapidly destroyed in their highly oxidized crusts and atmospheres. Thus PH_3 meets most criteria for a biosignature-gas search, but is challenging as many of its spectral features are strongly absorbed by Earth's atmosphere.

Motivated by these considerations, we exploited the PH_3 1–0 millimetre-waveband rotational transition that can absorb against optically thick layers of Venus's atmosphere. Long-standing speculations consider aerial biospheres in the high-altitude cloud decks[16,17], where conditions have some similarity to ecosystems making PH_3 on Earth[18]. We exploited good instrument sensitivity, 25 yr after the first millimetre-waveband exploration of Solar System PH_3 (in Saturn's atmosphere[19]). We proposed a 'toy model' experiment that could set abundance limits of the order of parts per billion on Venus, comparable to PH_3 production of some anaerobic Earth ecosystems[10]. The aim was a benchmark for future developments, but unexpectedly, our initial observations suggested a detectable amount of Venusian PH_3 was present.

We present next the discovery data and confirmation (and preliminary mapping) by follow-up observations, and rule out line contamination. We then address whether gas reactions, photo/geochemical reactions or exogenous non-equilibrium input could plausibly produce PH_3 on Venus.

Results

The PH_3 1–0 rotational transition at 1.123 mm wavelength was initially sought with the James Clerk Maxwell Telescope (JCMT), in observations of Venus over five mornings in June 2017. The

[1]School of Physics and Astronomy, Cardiff University, Cardiff, UK. [2]Institute of Astronomy, University of Cambridge, Cambridge, UK. [3]Jodrell Bank Centre for Astrophysics, Department of Physics and Astronomy, The University of Manchester, Manchester, UK. [4]Department of Earth, Atmospheric, and Planetary Sciences, Massachusetts Institute of Technology, Cambridge, MA, USA. [5]Department of Earth Sciences, University of Cambridge, Cambridge, UK. [6]Cavendish Astrophysics, University of Cambridge, Cambridge, UK. [7]MRC Laboratory of Molecular Biology, Cambridge, UK. [8]Department of Astrophysics and Atmospheric Science, Kyoto Sangyo University, Kyoto, Japan. [9]Department of Physics, Imperial College London, London, UK. [10]Royal Observatory Greenwich, London, UK. [11]School of Physical Sciences, The Open University, Milton Keynes, UK. [12]East Asian Observatory, Hilo, HI, USA. [13]Present address: Department of Physics and Kavli Institute for Astrophysics and Space Research, Massachusetts Institute of Technology, Cambridge, MA, USA. [14]Present address: Department of Aeronautics and Astronautics, Massachusetts Institute of Technology, Cambridge, MA, USA. ✉e-mail: greavesj1@cardiff.ac.uk

Table 1 | Properties of the PH_3 absorption line for regions of Venus's atmosphere

Facility (epoch)	Area of planet	l:c ratio (10^{-4})	Centroid (km s^{-1})	FWHM (km s^{-1})	Signal-to-noise ratio	Notes
JCMT (June 2017)	Whole planet	−2.5 ± 0.8 (−2.2, −3.1)	−0.2 ± 1.1 (−0.3 ± 1.2, −0.3 ± 0.9)	3.6 ± 1.2 (2.8 ± 1.0, 8.2 ± 2.3)	4.3 (3.0, 6.7)	$\|v\|$ = 5 km s^{-1} ($\|v\|$ = 2 km s^{-1}, 8 km s^{-1} for systematics)
ALMA (March 2019)	Whole planet	−0.87 ± 0.11	+0.7 ± 0.3 (+0.3 ± 0.3)	4.1 ± 0.5	13.3	$\|v\|$ = 5 km s^{-1} (linear fit for systematic)
	Equator (15° S–15° N)	−0.39 ± 0.14	+0.7 ± 0.9 (−0.0 ± 0.4)	4.8 ± 1.8	5.0	As for whole planet
	Mid-latitude (15–60° S + 15–60° N)	−1.26 ± 0.14	+0.7 ± 0.3 (+0.4 ± 0.3)	4.1 ± 0.6	14.5	As for whole planet
	Polar (60–90° S + 60–90° N)	(3σ: −0.29)	-	-	-	Limit for 10 km s^{-1} bins

Measurement errors are 1σ, and systematic errors are differences of the means and the mean values in brackets, the latter being obtained with the data-processing modifications stated in the 'Notes' column. l:c ratios are measured at the line minimum, for 1.1 km s^{-1} spectral bins that are in common to both datasets. Centroid velocities are referenced to the PH_3 1–0 line identification. Lines were fitted with Lorentzian profiles over ±10 km s^{-1} to estimate the full-width at half-minima (FWHM). For JCMT, intensity-weighted velocity centroids and line-integrated signal-to-noise ratios (based on per-channel errors) were calculated over ±10 km s^{-1} velocity ranges. For ALMA, calculation ranges were restricted to ±5 km s^{-1} because of the complexity of spectral ripple (see Extended Data Fig. 4), and centroids in brackets are for comparison, from a simplified linear fit immediately adjacent to the absorption. In all other cases, results are from spectra in Figs. 1 and 2, after the removal of polynomial baselines of order 8 (JCMT) and 12 (ALMA). We verified that high-order fitting does not produce artefact lines at arbitrary positions in the passband (Extended Data Fig. 4).

single-point spectra cover the whole planet (limb down-weighted by ~50% within the telescope beam). Absorption lines from the cloud decks were sought against the quasi-continuum created by overlapping broad emission features from the deeper, opaque atmosphere.

The main limitation at a small line-to-continuum ratio (hereafter, l:c ratio) was spectral 'ripple', from artefacts such as signal reflections. We identified three issues (see 'JCMT data reduction' in Methods), with the most problematic being high-frequency ripple drifting within observations in a manner hard to remove even in Fourier space (Extended Data Fig. 1). We thus followed an approach standardized over several decades[20], fitting amplitude-versus-wavelength polynomials to the ripples (in 140 spectra). The passband was truncated to 100 km s^{-1} to avoid using high polynomial orders. (Order is based on the number N of 'bumps' in the ripple pattern; fitting is optimal with order $N+1$ and negligibly improved at increased order. A wider band includes more 'bumps', increasing N. For minimum freedom, a linear fit can be employed immediately around the line candidate, ignoring the remaining passband—see Table 1 for resulting systematic differences.) We explored a range of solutions with the spectra flattened outside a velocity interval within which absorption is allowed. (The polynomial must be interpolated across an interval, as if fitted to the complete band it will always remove a line candidate, given freedom to increase order.) These interpolation intervals ranged from very narrow, preserving only the line core (predicted by our radiative transfer models, Fig. 1), up to a Fourier-defined limit above which negative-sign artefacts can mimic an absorption line. Details are in Methods, with the reduction script in Supplementary Software 1. The spectra were also reduced completely independently by a second team member, via a minimal-processing method that collapses the data stack down the time axis and fits a one-step, low-order polynomial; this gave a similar output spectrum but with a lower signal-to-noise ratio.

In our co-added spectrum (Fig. 1), we saw candidate PH_3 1–0 absorption, with the signal-to-noise ratio varying over ~3–7, depending on the velocity-interval selection. The feature is consistent with Venus's velocity, but is not precisely characterized (Table 1). This potentially allows for the feature to be a weak residual artefact, or a transition of another molecule at a nearby wavelength.

We thus sought confirmation of the same transition, with independent technology and improved signal-to-noise ratio, using the Atacama Large Millimetre/submillimetre Array (ALMA) in March 2019. In principle, ALMA's arcsecond-scale resolution would allow detailed mapping of the planet's atmosphere. In practice, interferometric response to a large bright planet produced artefactual spectral ripples varying from baseline to baseline (and not eliminated by bandpass calibration). This systematic was greatly reduced, before imaging, by excluding all telescope-to-telescope baselines <33 m in length. This was necessary for dynamic range and was the only substantial departure from the standard ALMA 'QA2' approach[21] to data reduction (see 'ALMA data reduction' in Methods, Extended Data Figs. 2–4 and Supplementary Software 2–4). While bandpass calibration using Jupiter's moon Callisto was not fully sufficient, the dynamic range achieved was still substantially higher than ALMA's specification (~10^{-3} in l:c ratio, without the techniques we used to reduce systematics, and which we verified did not produce spurious features). To eliminate residual ripple from the extracted spectra, we tested polynomial fitting strategies with orders ranging from 12 (optimal for an 80 km s^{-1} passband, Fig. 2), down to 1 (fitting only around the line candidate). The resulting systematic uncertainties are summarized in Table 1.

We also checked for robustness by searching simultaneously for deuterated water (HDO) known to be present on Venus. The HDO $2_{2,0}$–$3_{1,3}$ line at 1.126 mm wavelength was detected (Extended Data Fig. 5: preliminary output from manual 'QA2' scripts), with a line profile well fitted by our radiative transfer model, and a Venus-normal water abundance (see 'ALMA data reduction' in Methods). Simultaneous wider-bandpass settings also allowed us to set upper limits on other chemical species—transitions here could be a check on possible contaminants, that is, constrain transitions close in wavelength to the line we identify as PH_3 1–0. The wide-bandpass tuning centred on this PH_3 transition provided a further reproducibility check. These data have greater problems with spectral ripple than in the narrow-bandpass settings, but the PH_3 line was recovered (Extended Data Fig. 6).

The effect of removal of short-baseline ALMA data is that line signals from areas smooth on scales >4 arcsec are substantially diluted. Thus our l:c ratio corresponds to lower limits of PH_3 abundance (but detection significance is not affected; these values are as stated in Table 1). Further, the steep flux density gradients at the limb resulted in more flux being recovered here. To ensure that results are robust, we did not attempt to interpret any absorption spectra over arcsecond scales (Extended Data Fig. 3). To mitigate for the bias in better sampling the limb, the spectra in Fig. 2 are all averages from 'side-to-side' strips across the planet.

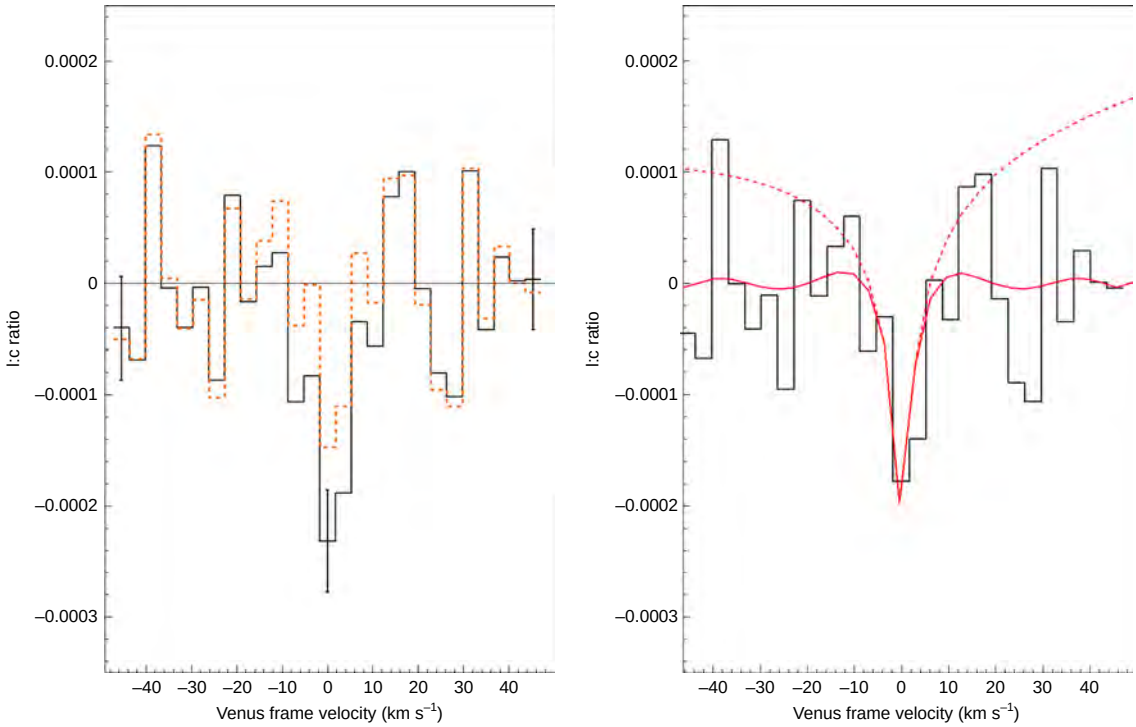

Fig. 1 | Spectra of PH_3 1–0 in Venus's atmosphere as observed with the JCMT. Axes are l:c ratio against Doppler-shifted velocity referenced to the PH_3 wavelength. Left: the least and most conservative solutions after fitting and removing spectral ripple (see 'JCMT data reduction' in Methods), with the residual line present inside velocity ranges of $|v| = 8\,km\,s^{-1}$ (solid, black) and $|v| = 2\,km\,s^{-1}$ (dashed, orange). The data have been binned for clarity into histograms (that is, bars denoting averages) on the *x* axis; representative 1σ error bars are 0.46×10^{-4} in l:c ratio per $3.5\,km\,s^{-1}$ spectral bin. Error bars indicate the dispersion within each channel from 140 co-added input spectra; channel-to-channel dispersion is higher by ~40%, attributable to residual ripple, and contributing to the range of signal-to-noise ratio (Table 1). Right: the adopted mid-range solution with $|v| = 5\,km\,s^{-1}$ (histogram), overlaid with our model for 20 ppb abundance by volume. The solid red curve shows this model after processing with the same spectral fitting as used for the data. The line wings and continuum slope have thus been removed from the original model (bottom dashed red curve). As the spectral fitting forces the line wings towards zero, only the range $\pm 10\,km\,s^{-1}$ around Venus's velocity was used in line characterization (Table 1).

The ALMA data confirm the detection of absorption at the PH_3 1–0 wavelength. All line-centroid velocities are consistent with Venus's velocity within −0.2 to +0.7 $km\,s^{-1}$ (around 10% of the line width), with best measurement precision at $\pm 0.3\,km\,s^{-1}$ and systematics of ~0.1–0.7 $km\,s^{-1}$ (Table 1). For this degree of coincidence of apparent velocity, any contaminating transition from another chemical species would have to coincide in rest wavelength with PH_3 1–0 within ~10^{-6}.

The data above represent the candidate discovery of PH_3 on Venus. Because of the very high l:c ratio sensitivity required, we tested robustness through several routes. In particular, we analysed data from both facilities by a range of methods and estimated systematic uncertainties.

The JCMT and ALMA whole-planet spectra agree in line velocity and width, and are consistent in line depth after taking into account ALMA's spatial filtering (hence, no temporal variation in PH_3 abundance needs to be invoked over 2017–2019). We considered ALMA's maximum line loss, in the case of a PH_3 distribution as uniform as the almost-smooth continuum (Extended Data Fig. 2). Comparing the ALMA continuum signals with/without baselines of <33 m in the data reduction, we found filtering losses varying from a net 60% in our polar regions to 92% for our equatorial band. Correcting the whole-planet line signal by this method, the l:c ratio could rise from -0.9×10^{-4} to -4.9×10^{-4}, values bracketing -2.5×10^{-4} from the JCMT. Hence, the ALMA and JCMT lines differ by factors of at most two to three, with agreement possible if the PH_3 is distributed on intermediate scales (between highly uniform and small patches).

Finally, for robustness, we considered the possibility of a 'double false positive', where a negative dip occurs in both datasets near the Venusian velocity. Comparing the data before the final processing step of polynomial fitting takes place, Fig. 3 shows that no other coincidences of absorption-line-like features occur in the JCMT and ALMA spectra.

Next, we examined whether transitions from gases other than PH_3 might absorb at nearby wavelengths. The only plausible candidate (Supplementary Table 1) is a SO_2 transition offset by $+1.3\,km\,s^{-1}$ in the reference frame of PH_3 1–0. This is expected to produce a weak line in the cloud decks, with its lower quantum level at energy >600 K not being highly populated in <300 K gas. SO_2 absorptions from energy levels at ~100 K have been detected[22], and we searched for one such transition in our simultaneous ALMA wideband data. We did not detect significant absorption (Fig. 4a). Given this observation, our radiative transfer model predicts what the maximum absorption from the 'contaminant' SO_2 line would be, finding a weak l:c ratio, not deeper than -0.2×10^{-4} (Fig. 4b). SO_2 can contribute a maximum of <10% to the l:c ratio integrated over $\pm 5\,km\,s^{-1}$ and shift the line centroid by $<0.1\,km\,s^{-1}$. These results are abundance and model independent. The contaminant SO_2 line could only 'mimic' the PH_3 feature while the wideband SO_2 line remained undetected if the gas was more than twice as hot as measured in the upper clouds—that is, at temperatures found only at much lower altitudes than our data probe.

We are unable to find another chemical species (known in current databases[23–26]) besides PH_3 that can explain the observed features. We conclude that the candidate detection of PH_3 is robust, for

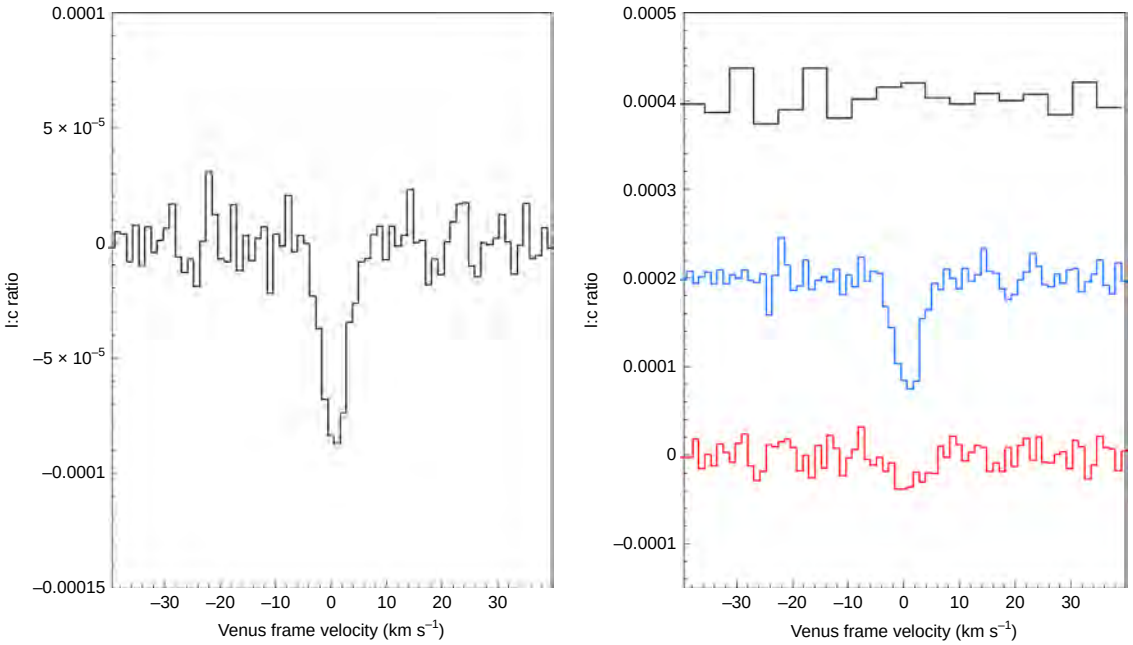

Fig. 2 | Spectra of Venus obtained with ALMA. Left: the PH_3 1–0 spectrum of the whole planet, with 1σ errors (here channel to channel) of 0.11×10^{-4} per 1.1 km s^{-1} spectral bin. Right: spectra of the polar (histogram in black), mid-latitude (in blue) and equatorial (in red) zones, as defined in Table 1. Spectra have been offset vertically for clarity, and the polar spectrum was binned in velocity to obtain a deeper upper limit. Line wings are forced towards zero outside $|v| = 5$ km s^{-1} in these spectra, and only this range was used in characterization (Table 1 and 'ALMA data reduction' in Methods).

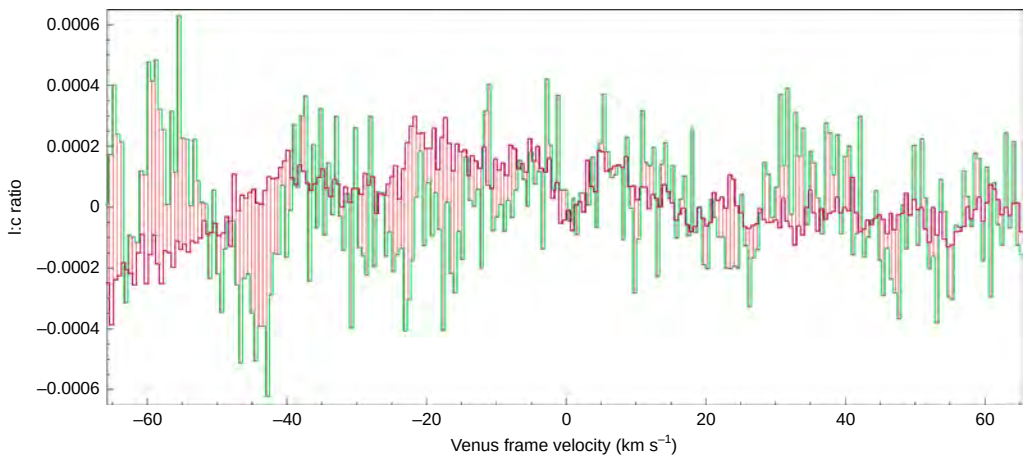

Fig. 3 | JCMT and ALMA whole-planet spectra across the full passband common to both datasets. These are the co-added JCMT (green) and ALMA (purple) spectra before removal of a final polynomial baseline. The ALMA spectrum has been scaled up by a factor of three, the estimated loss for spatial filtering (compare the first two I:c ratio entries in Table 1). Vertical red bars connect the JCMT and ALMA data (bin centres agree in velocity within ±0.2 km s^{-1}). A line feature is considered to be real where this dispersion (red bar) is low; only the candidate PH_3 feature around $v = 0$ km s^{-1} meets this criterion. Other 'dips' across the band have high dispersion (they occur in only one dataset) or cover only a few contiguous bins (much less than the line width expected for Venus's upper-atmosphere absorption).

four main reasons. First, the absorption has been seen, at comparable line depth, with two independent facilities; second, line measurements are consistent under varied and independent processing methods; third, overlap of spectra from the two facilities shows no other such consistent negative features; and fourth, there is no other known reasonable candidate transition for the absorption other than PH_3.

The few km s^{-1} widths of the PH_3 spectra are typical of absorptions from the upper atmosphere of Venus[22]. Inversion techniques[27] can convert line profiles into a vertical molecular distribution, but this is challenging here due to uncertainties in PH_3 line dilution and pressure broadening. As the continuum against which we see absorption[28] arises at altitudes of ~53–61 km (Extended Data Fig. 2), in the middle/upper cloud deck layers[17], the PH_3 molecules observed must be at least this high up. Here the clouds are 'temperate', at up to ~30 °C, and with pressures up to ~0.5 bar (ref. [29]). However, PH_3 could form at lower (warmer) altitudes and then diffuse upwards.

PH_3 is detected most strongly at mid-latitudes and is not detected at the poles (Table 1). The equatorial zone appears to absorb more weakly than mid-latitudes, but equatorial and mid-latitude values

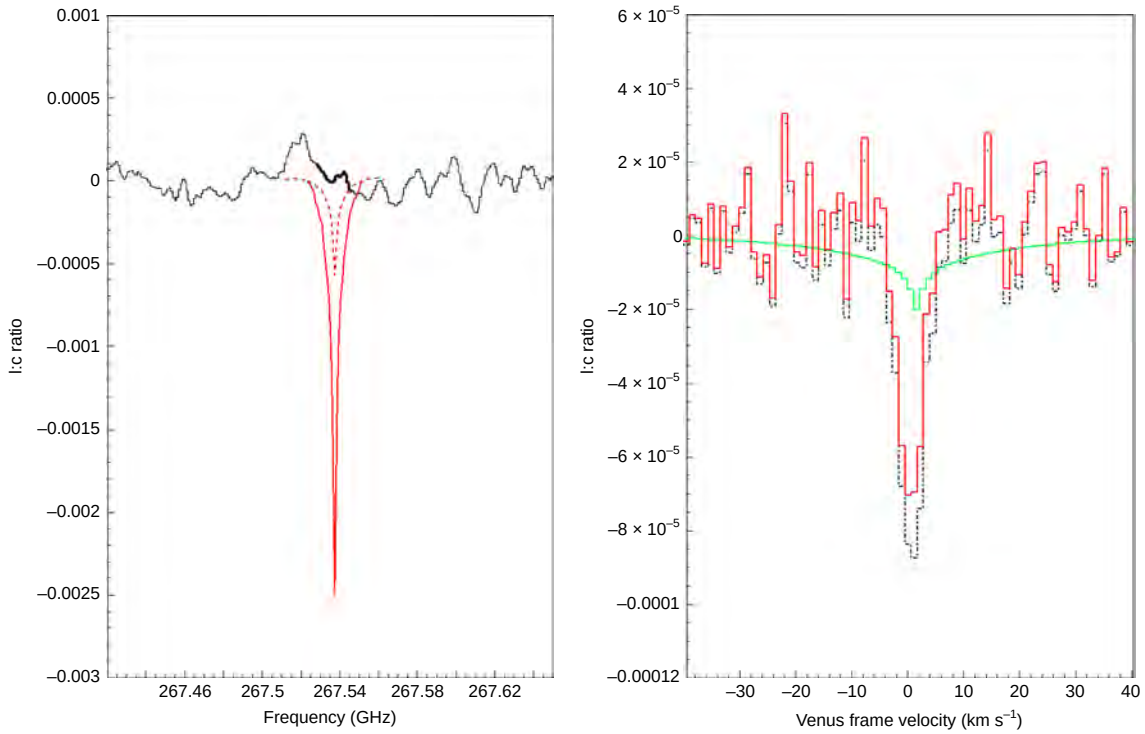

Fig. 4 | The process of estimating SO_2 contamination of the PH_3 line. Left: a section of ALMA wideband data (whole planet, after a third-order polynomial correcting for broad curvature has been removed), around the SO_2 $13_{3,11}$–$13_{2,12}$ rest frequency of 267.53745 GHz (wavelength ~1.121 mm). The thicker histogram over the ±10 km s^{-1} range illustrates that SO_2 absorption is not seen. The red dashed curve is an SO_2 10 ppb model, after subtracting a polynomial forcing line wings towards zero outside $|v| = \pm 10$ km s^{-1}. The 10 ppb model was chosen to reproduce the maximum line depth possible within the data, approximating to the peak-to-peak spectral ripple. The red solid curve is scaled up to show the amplitude this SO_2 line would need to have if the line we identify as PH_3 1–0 is instead all attributed to the SO_2 $30_{9,21}$–$31_{8,24}$ transition. Right: our model for the maximum allowed SO_2 $30_{9,21}$–$31_{8,24}$ contribution is re-plotted as a green histogram; this is, the red dashed model of the left panel, but without any polynomial subtraction. The PH_3 whole-planet spectrum of Fig. 2 (here a black dot-dashed histogram) is then re-plotted (red solid histogram) after subtraction of this maximized model of SO_2 $30_{9,21}$–$31_{8,24}$.

could agree if corrections are made for spatial filtering. Following the method above (treating gas as though distributed like the continuum), then the l:c ratio can be as deep as -4.6×10^{-4} for the equator and -5.8×10^{-4} for mid-latitudes, in agreement at the 1σ bounds (both $\pm 0.7 \times 10^{-4}$). However, for the polar caps, the l:c ratio cannot exceed -0.7×10^{-4} by this method (as small limb regions are the least affected by missing short-baseline data). Our latitude ranges were set empirically, to maximize contrasts in the l:c ratio, so may not represent physical zones. We were unable to compare bands of longitude (for example, for any effects of solar angle), as regions nearer the limb had increasing issues of noise and spectral ripple (Extended Data Fig. 3).

The abundance of PH_3 in Venus's atmosphere was estimated by comparing a model line to the JCMT spectrum, which has the least signal losses. The radiative transfer in Venus's atmosphere was calculated using a spherical, multilayered model, with temperature and pressure profiles from the Venus International Reference Atmosphere (VIRA). Molecular absorptions are calculated by a line-by-line code, including CO_2 continuum-induced opacity. JCMT beam dilution is included. The abundance calculated is ~20 ppb (Fig. 1). The model's major uncertainty is in the CO_2 pressure-broadening coefficient, which has not been measured for PH_3. We take PH_3 1–0 line broadening coefficients to range from 0.186 cm^{-1} atm^{-1}, (our theoretical estimate) to 0.286 cm^{-1} atm^{-1} (the measured value for the CO_2 broadening of the NH_3 1–0 line). Ammonia and PH_3 share many similarities (see 'Abundance retrieval' in Methods), and can be expected to have comparable broadening properties[30,31]. With this range of coefficients, derived abundances range from ~20 ppb (using our theoretical estimate) up to ~30 ppb (using the proxy NH_3 broadening). In addition, uncertainty in the l:c ratio in the JCMT spectrum contributes ~30% (±6 ppb), with additional shifts of −2,+5 ppb possible from systematics (Table 1).

The presence of even a few parts per billion of PH_3 is completely unexpected for an oxidized atmosphere (where oxygen-containing compounds greatly dominate over hydrogen-containing ones). We review all scenarios that could plausibly create PH_3, given established knowledge of Venus.

The presence of PH_3 implies an atmospheric, surface or subsurface source of phosphorus, or delivery from interplanetary space. The only measured values of atmospheric phosphorus on Venus come from Vega descent probes[32], which were only sensitive to phosphorus as an element, so its chemical speciation is not known. No phosphorus species have been reported at the planetary surface.

The bulk of any phosphorus present in Venus' atmosphere or surface is expected as oxidized forms of phosphorus, for example, phosphates. Considering such forms, and adopting Vega abundance data (the highest inferred value, most favourable for PH_3 production), we calculate whether equilibrium thermodynamics under conditions relevant to the Venusian atmosphere, surface and subsurface can provide ~10 ppb of PH_3. (We adopt a lower-bound adequately fitting the JCMT data, to find the most readily achievable thermodynamic solution.) We find that PH_3 formation is not favoured even considering ~75 relevant reactions under thousands of conditions encompassing any likely atmosphere, surface or subsurface properties (temperatures of 270–1,500 K, atmospheric and subsurface pressures of 0.25–10,000 bar, wide range of concentrations of

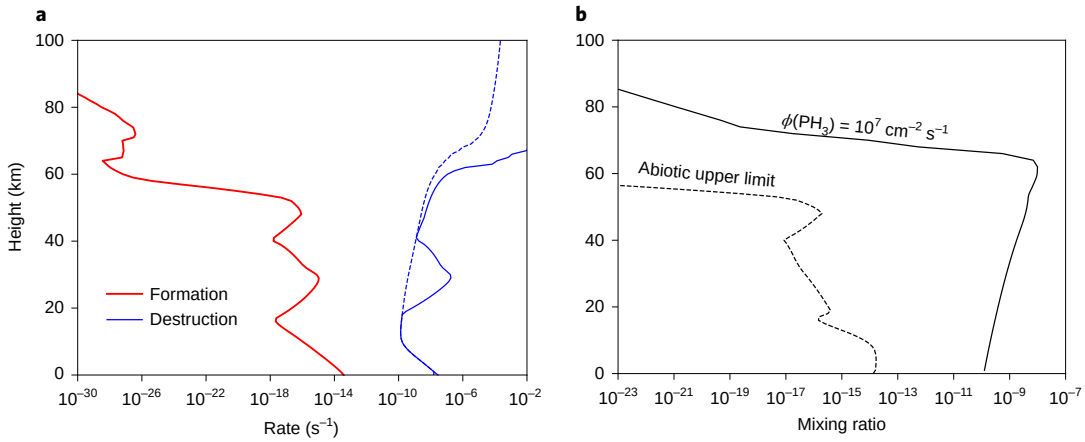

Fig. 5 | Predicted maximum photochemical production of PH_3 found to be insufficient to explain observations by more than four orders of magnitude. a, Upper limits of the predicted photochemical production rates of PH_3 (excluding transport; red curve, s^{-1}) compared with photochemical destruction rates (blue curve, s^{-1}), including radicals and atoms (blue solid) and ignoring radicals and atoms (blue dashed), as a function of height (km). See kinetic network of Extended Data Fig. 7. **b**, Mixing ratio of PH_3 as a function of atmospheric height (km), for a production flux ($\phi(PH_3)$) within the cloud layer (~55–65 km) of 10^7 cm^{-2} s^{-1} (solid curve), compared with the predicted steady-state abiotic upper limit (dashed curve). See kinetic network of Extended Data Fig. 7.

reactants). The free energy of reactions falls short by anywhere from 10 to 400 kJ mol^{-1} (see 'Potential pathways to PH_3 production' in Methods, Supplementary Information and Extended Data Fig. 7). In particular, we quantitatively rule out the hydrolysis of geological or meteoritic phosphide as the source of Venusian PH_3. We also rule out the formation of phosphorous acid (H_3PO_3). While phosphorous acid can disproportionate to PH_3 on heating, its formation under Venus temperatures and pressures would require quite unrealistic conditions, such as an atmosphere composed almost entirely of hydrogen (for details, see Supplementary Information).

The lifetime of PH_3 on Venus is key for understanding production rates that would lead to accumulation of few-ppb concentrations. This lifetime will be much longer than on Earth, the atmosphere of which contains substantial molecular oxygen and its photochemically generated radicals. The lifetime above 80 km on Venus (in the mesosphere[22]) is consistently predicted by models to be <10^3 s, primarily due to high concentrations of radicals that react with, and destroy, PH_3. Near the atmosphere's base, the estimated lifetime is ~10^8 s due to thermal decomposition (collisional destruction) mechanisms. Lifetimes are very poorly constrained at intermediate altitudes (<80 km), being dependent on abundances of trace radical species, especially chlorine. These lifetimes are uncertain by orders of magnitude, but are substantially longer than the time for PH_3 to be mixed from the surface to 80 km (<10^3 yr). The lifetime of PH_3 in the atmosphere is thus no longer than 10^3 yr, either because it is destroyed more quickly or because it is transported to a region where it is rapidly destroyed (see 'Photochemical model' in Methods, Supplementary Information, Extended Data Figs. 8 and 9, and Supplementary Tables 2 and 3).

We estimate the outgassing flux of PH_3 needed to maintain ~10 ppb levels, taking the column of PH_3 derived from observations and dividing this by the chemical lifetime of PH_3 in Venus's atmosphere (Fig. 5). The total outgassing flux necessary to explain ~10 ppb of PH_3 is ~10^6–10^7 molecules cm^{-2} s^{-1} (shorter lifetimes would lead to higher flux requirements). Photochemically driven reactions in Venus's atmosphere cannot produce PH_3 at this rate. To generate PH_3 from oxidized phosphorus species, photochemically generated radicals have to reduce the phosphorus by abstracting oxygen and adding hydrogen—requiring reactions predominantly with H, but also with O and OH radicals. Hydrogen radicals are rare in Venus's atmosphere because of low concentrations of potential hydrogen sources (species such as H_2O and H_2S that are ultraviolet photolyzed to produce H radicals). We model a network of forward reactions (that is, from oxidized phosphorus species to PH_3), not only as a conservative maximum possible production rate for PH_3 but also because many of the back-reaction rates are not known. We find that the reaction rates of H radicals with oxidized phosphorus species are too slow by factors of 10^4–10^6 under the temperatures and concentrations in the Venusian atmosphere (Fig. 5).

Energetic events are also not an effective route to making PH_3. Lightning may occur on Venus, but at sub-Earth activity levels[33]. We find that PH_3 production by Venusian lightning would fall short of few-ppb abundance by factors of 10^7 or more. Similarly, there would need to be >200 times as much volcanic activity on Venus as on Earth to inject enough PH_3 into the atmosphere (up to ~10^8 times, depending on assumptions about mantle rock chemistry). Orbiter topographical studies have suggested there are not many large, active, volcanic hotspots on Venus[34]. Meteoritic delivery adds at most a few tonnes of phosphorus per year (for Earth-like accretion of meteorites). Exotic processes such as large-scale tribochemical (frictional) processes and solar wind protons also only generate PH_3 in negligible quantities (W. Bains et al., manuscript in preparation, submitted to *Astrobiology* as 'Phosphine on Venus cannot be explained by conventional processes'; also see Extended Data Fig. 10).

Discussion

If no known chemical process can explain PH_3 within the upper atmosphere of Venus, then it must be produced by a process not previously considered plausible for Venusian conditions. This could be unknown photochemistry or geochemistry, or possibly life. Information is lacking—as an example, the photochemistry of Venusian cloud droplets is almost completely unknown. Hence a possible droplet-phase photochemical source for PH_3 must be considered (even though PH_3 is oxidized by sulfuric acid). Questions of why hypothetical organisms on Venus might make PH_3 are also highly speculative (see 'PH_3 and hypotheses on Venusian life' in Methods and Supplementary Information).

Quantitatively, we can note that the production rates of ~10^6–10^7 molecules cm^{-2} s^{-1} inferred above are lower than the production by some terrestrial ecologies, which make the gas[10] at 10^7–10^8 PH_3 cm^{-2} s^{-1}. Considering also distribution, the PH_3 on

Venus is at or near temperate altitudes, and is also lacking around the polar caps. It has been suggested[35] that the mid-latitude Hadley circulation cells offer the most stable environment for life, with circulation times of 70–90 days being adequate for reproduction of (Earth analogue) microbes. PH_3 is not detected by ALMA above an ~60° latitude bound, agreeing within ~10° with the proposed upper Hadley-cell boundary[36] where gas circulates to lower altitudes. However, further work on diffusion processes (Extended Data Fig. 9) is desirable.

In the context of Solar System biosignature searches, our observations of the PH_3 1–0 line have proved powerful for modest facility time (<10 h on-source). The PH_3 abundance is well-enough constrained (within factors ~2–3) for worthwhile modelling, and no ad hoc introduction of temporal effects is needed. We have ruled out contaminants, and narrow lines mean that a currently unknown chemical species would need to have a transition at an extremely nearby wavelength to mimic the PH_3 1–0 line. However, confirmation is always important for a single-transition detection. Other PH_3 transitions should be sought, although observing higher-frequency spectral features may require a future large air- or space-borne telescope.

Even if confirmed, we emphasize that the detection of PH_3 is not robust evidence for life, only for anomalous and unexplained chemistry. There are substantial conceptual problems for the idea of life in Venus's clouds—the environment is extremely dehydrating as well as hyperacidic. However, we have ruled out many chemical routes to PH_3, with the most likely ones falling short by four to eight orders of magnitude (Extended Data Fig. 10). To further discriminate between unknown photochemical and/or geological processes as the source of Venusian PH_3, or to determine whether there is life in the clouds of Venus, substantial modelling and experimentation will be important. Ultimately, a solution could come from revisiting Venus for in situ measurements or aerosol return.

Methods

JCMT data reduction. The reduction was all performed offline, within the Starlink Project software suite[37]. The manipulation of timestream data used KAPPA[38], the cube was made in SMURF[39] and the final spectra were constructed in SPLAT[40]. The software is open access and is supported by the East Asian Observatory. Our data processing can be reproduced using the script in Supplementary Software 1.

Standard methods in millimetre-waveband single-dish spectroscopy were used to process 140 JCMT spectra, finally reaching a dynamic range better than 10^4 for the l:c ratio. Ref. [41] describes the specifics of observing Venus with the JCMT; we omitted their telluric correction step as any trace terrestrial PH_3 would be suppressed by beam switching and calibration, and offset in velocity by 13.5–14.1 km s^{-1} at the time of our Venus observations.

Undulations in amplitude versus frequency, equivalently Doppler-shifted velocity, occur across the passband. Time-delayed signals due to reflections of the bright planetary continuum (for example, reflection off the calibration cold load not be seen when observing the sky) yield difference spectra with residual ripples. Wave-period analysis[42] suggests two major effects from reflections within the receiver cabin (for details, see 'JCMT data reduction' in Supplementary Information). Both effects were removed by fitting polynomial functions, with 'troughs' much broader than the core of the absorption line we seek (Extended Data Fig. 1). However, this subtraction removes the line wings, expected to span tens of megahertz; after this step, the line-centre l:c ratio value underestimates the true line depth (Fig. 1b).

A third ripple has troughs of comparable width to the line and similar amplitude (for origins, see Supplementary Information), sometimes shifting phase within each ~30 min observation (Extended Data Fig. 1). For ~16 waves across a 250 MHz passband (281 km s^{-1} at 266.9445 GHz), each half-wave occupies ~9 km s^{-1}, so an artefact 'trough' is similar in width to model lines. We applied polynomial fits on a subscan basis, restricting the passband to avoid use of high orders. Over 100 km s^{-1}, 10 or 11 peaks/troughs are expected, with 1 or 2 being interpolated across (overlaying the line). The polynomial interpolates over a user-selected region around the line velocity, to avoid fitting (and removing) the line as if it were an artefact. This interpolation region can not exceed ~18 km s^{-1} or the polynomial has no information to detect, for example, a downwards trend between two peaks. The polynomials finally adopted were of eighth order, an empirical minimum that reasonably flattened the baseline. This order is just below the expected value of $(N+1)=9$–11, for $N=8$–10 peaks/troughs outside the interpolation region.

The possible interpolation regions within model and data constraints span ~4–16 km s^{-1}. Figure 1b adopts $|v|=5$ km s^{-1}, that is, fitted at velocities $v<-5$ km s^{-1} and $v>+5$ km s^{-1} with respect to Venus, and interpolated over −5 to +5 km s^{-1}. The alternate $|v|$ provide minimum and maximum solutions to line depth (Fig. 1a). The smallest $|v|$ value of 2 km s^{-1} is very strict and allows only the highest-confidence spectral bins to be detected; this range falls below the half-width at half-minimum in our line model (red dashed curve, Fig. 1b). The largest $|v|$ value of 8 km s^{-1} is an approximate upper bound, as for larger $|v|$, polynomial amplitudes become greater in the passband centre than at all other velocities. This 'bulge' appears unrealistic, and can artificially force the line to be deeper and wider. These two approaches bracket line depths that can be obtained from the data.

For each subobservation, we calculated [(data + continuum)/(polynomial + continuum) − 1], in a standard approach where division by the baseline fit performs better than subtraction. 'Data' is the residual after the first two polynomial subtractions, 'polynomial' is the spectral baseline in the third fitting step, and 'continuum' is the mean signal before any subtractions. Our script yields 140 subobservation l:c ratio spectra plus a co-add weighted by per-observation system temperature. Standard deviations are generated on a per-channel basis from the dispersion of 140 input values, and agree within ~1% from channel to channel.

ALMA data reduction. Details of data acquisition are given in Supplementary Information. Important steps included choosing local oscillator settings to minimize instrumental effects, and accurately tracking positions of Venus and the calibrator Callisto. Their flux densities (ignoring spectral lines) were set using the NASA ephemeris and the 'Butler-JPL-Horizons 2012' standard[43]. Frequency channels were mapped to velocity channels in processing using the Venus ephemeris, so that in the final image cubes, 0 km s^{-1} corresponds to line frequency in the planetary-motion frame of Venus.

The UK ALMA Regional Centre Node retrieved the raw data from the ALMA Science Archive and ran the standard manually generated calibration script ('QA2' in ALMA quality assurance documentation and technical handbook) on each execution block. Calibration and imaging followed normal imaging procedures but with a few modifications:

- For flux scale and bandpass calibration involving Callisto, baselines shorter than 180 klambda (~200 m), just inside the first null, were used, providing at least one baseline for every antenna to the reference antenna.
- Viewing the calibrated visibility spectrum and imaging Venus revealed a spectral ripple, which was worst on short baselines. The absorption feature is still seen, but these baseline-dependent errors impede accurate image analysis. There was an insufficient signal-to-noise ratio on Callisto for baseline-dependent calibration, so we flagged all baselines <33 m at an early stage (choice described in Supplementary Information).

Absorption is not present if Callisto is reduced in a similar fashion (excluding short baselines; same channel selection for continuum subtraction from visibilities). The bandpass correction using Callisto used an 8 MHz channel averaging, that is, such a narrow line would have remained in Callisto, but this was not seen. Hence, the PH_3 signal is associated with Venus, not the calibrator.

The initial calibration scripts used to produce the data cubes that we analysed are provided as Supplementary Software 2 and 3. After applying calibration, we combined all Venus data for each spectral configuration, here describing processing of the wideband and narrowband configurations centred on 266.9 GHz.

We performed time-dependent phase self-calibration using continuum-only channels and applied the solutions to all channels. We excluded the central channels (and, for wideband, channels covering a telluric line), and subtracted a first-order fit to the continuum from each visibility dataset.

Separately, wideband data with all baselines present were processed similarly up to applying phase self-calibration, and used to produce a continuum image, diameter 15.36 arcsec (verifying the positional accuracy of the ephemeris and tracking). We used a mask of this size, centred on Venus (Extended Data Fig. 2) in imaging the continuum-subtracted narrowband cube.

ALMA spectra were extracted using CASA. Inspection of a grid of spectra (Extended Data Fig. 3) showed a residual ripple, varying in shape at adjacent grid points (regardless of grid spacing). Ripples are especially pronounced for spectra at the planetary limb. Gradients across the field are apparent when viewing individual channels. These artefacts appear to arise from the high brightness of Venus (almost filling the primary beam), as a net spectrum surrounding (but excluding) the planet showed a ripple that is the inversion (opposite amplitude sign) of the ripple in the whole-planet spectrum.

The best mitigation was to extract net-spectra for bands of latitude across the planet. All such bands were drawn in the CASA viewer (Extended Data Fig. 2), with connection points estimated as positioned within two 0.16 arcsec pixels, below the restoring-beam scale. This 'side-to-side' (zonal mean) methodology takes advantage of gradients such that ripples partially cancel, and PH_3 lines becomes visible over extended regions. Resulting spectra (Fig. 2) have least noise around the equator, and are noisiest/most-ripply towards the poles (areas dominated by beams at the limb). Attempts to construct similar bands spanning longitude ranges did not make spectra that were satisfactorily stable, that is, they changed substantially

with sub-beam shifts of boundary points. Longitudes at the limb exhibit more spectral ripple, and also gradients along this axis appear not to self-cancel ripples.

The final region-averaged spectra were analysed and plotted in SPLAT[40].

In producing final ALMA spectra (Fig. 2), we subtracted polynomial functions as for JCMT data, but only needed to do this once for each region-averaged spectrum. The flattest spectral baselines were obtained by restricting the passband to $\pm 40\,km\,s^{-1}$ from Venus's velocity, and interpolating across $|v| = 5\,km\,s^{-1}$. Polynomials of 12th order were necessary, higher than the 8th order JCMT fits; we verified that lower orders, for example, 11, yielded worse noise while higher orders, for example, 14, did not improve the noise. The spectra are shown in Extended Data Fig. 4 with the fits overlaid, to demonstrate that the PH_3 lines are distinct and unlikely to be subtraction artefacts.

As a robustness check, a preliminary reduction of the HDO transition observed simultaneously is shown in Extended Data Fig. 5. (Before a full investigation, we have only spectrally binned the narrowband data to flatten ripples and applied a first-order polynomial fit.) The same processing was applied to a model line from our radiative transfer code, for a HDO abundance set to 2.5 ppb (red curve). If HDO is smoothly distributed, this line will suffer losses from the missing ALMA short baselines, and so for losses, for example, comparable to the continuum signal, up to ~14 ppb of HDO is possible. The H_2O abundance would then be ~0.04–0.2 ppm, following ref. [22] for deuteration correction. This is within low-end water abundances reported from millimetre-waveband monitoring—values are strongly time variable, with detections at ~0.1–3.5 ppm (ref. [44]).

We verified PH_3 absorption in the wideband data, which are simultaneous (coming from the same photons). These spectra have substantial ripple (Extended Data Fig. 6), so are only minimally processed, via a first-order polynomial fit using velocity ranges of −20 to $-5\,km\,s^{-1}$ and +5 to $+20\,km\,s^{-1}$. In the wideband data, the PH_3 line is present but only of modest significance. The line minimum is ~50% deeper than in the narrowband data, with a velocity centroid at about $-0.9 \pm 0.6\,km\,s^{-1}$.

Calculation of SO_2 contamination. We also used the ALMA wideband tunings to search for other transitions, especially checking whether our PH_3 line candidate could be a mis-identification of a SO_2 feature. This SO_2 transition (Supplementary Table 1) would comprise absorption from a lower-level $J = 31$ rotational state, with J being the rotational quantum number. This energy state is at 613 K, and our wideband spectra also covered transitions from $J = 13$, 28 and 46, at energy levels of 93, 403 and 1,090 K, respectively. In principle, an excitation diagram of these three lines could yield an interplated flux of the $J = 31$ 'interloper', but in practice none of the transitions was detected. SO_2 lines from Venus even at energy levels of ~100 K are challenging, for example, noting 1/4 successful attempts in ref. [22] (with only half the antennas commissioned for their early ALMA run).

In our whole-planet wideband spectrum, we do not detect the most favourable SO_2 transition. We adopt a very generous upper limit on this line, allowing ~100% of peak-to-peak amplitude of nearby ripples (Fig. 4). In our radiative transfer model, this limit requires a SO_2 abundance of 10 ppb at ≥88 km, in reasonable agreement with ~16 ppb fitted to a previous mesospheric altitudes detection with ALMA[27] (and without attempting line-dilution corrections). Our model then predicts an l:c ratio $< 2 \times 10^{-5}$ for the 'interloper' $J = 31$ line minimum. After polynomial fitting to this model as for the observations, the l:c ratio integrated over $\pm 5\,km\,s^{-1}$ is only 8% of the feature identified as PH_3. After subtracting the maximized SO_2 contamination (Fig. 4), the velocity centroid of the residual moves towards zero as might be expected if the PH_3 identification is correct, but by $< 0.1\,km\,s^{-1}$. Figure 4 also demonstrates that SO_2 $J = 31$ cannot reproduce the entire line identified as PH_3, as the SO_2 $J = 13$ component would strongly violate the wideband limit.

Abundance retrieval. Radiative transfer in the Venus atmosphere is calculated assuming spherically homogeneous atmospheric layers. The atmosphere from the surface up to 140 km is divided into 1-km-depth layers, with a temperature profile from a Venus international reference model (VIRA), established from spacecraft temperature measurements. A vertically constant PH_3 mixing ratio is assumed here. Atmospheric opacity at each Venus altitude (Extended Data Fig. 2) is calculated with line-by-line computation of molecular lines (CO, SO_2, H_2O, PH_3…) and continuum opacity due to the collision-induced absorption of CO_2. Scattering due to cloud particles is omitted as negligible in our millimetre waveband. The 'emission angle effect' (longer line of sight at the limb of Venus) is included. Pencil-beam spectra are calculated with a fine grid along the radial direction of the Venus disk, accounting for emission angle, and then convolved with ALMA's synthesized beam (an elliptic Gaussian). Finally, spectra within the apparent disk are all integrated to obtain a disk-averaged model spectrum. For the JCMT simulation, the process was the same but it used the JCMT Gaussian beam size instead of ALMA's synthesis beam.

The largest source of uncertainty in the retrieved abundances is a lack of collisional broadening parameters for the PH_3 $J = 1$–0 transition. Ammonia is often used as proxy to PH_3 as the two molecules share many similarities, including comparably dense energy levels. In the absence of measurements for CO_2 broadening/shift effects on the PH_3 $J = 1$–0 line, we considered two alternatives: (1) measured CO_2 broadening effect of the NH_3 $J = 1$–0 line ($0.2862\,cm^{-1}\,atm^{-1}$), and (2) a theoretical value estimated from a ratio of known broadening of H_2/He for both PH_3 and NH_3 ($0.186\,cm^{-1}\,atm^{-1}$).

Photochemical model. Within the atmosphere of Venus, PH_3 is destroyed by photochemically generated radical species, by near-surface thermal decomposition and by photodissociation within/above the clouds. Since PH_3 itself scavenges chemically reactive radicals and atoms, for example, OH, H, O and Cl, the presence of PH_3 suppresses these species, increasing its lifetime. Previously published models of Venus's atmosphere did not include the scavenging effect of PH_3, so we developed our own model.

We employ the one-dimensional photochemistry diffusion code ARGO[45] to solve the atmospheric transport equation. For the ultraviolet transport, a 'mysterious absorber' is included[46]. For our chemical network, we use STAND2019[47], which includes H/C/N/O species, adding a limited S/Cl/P network relevant for Venus by adapting published low- and middle-atmosphere networks[46,48,49] and developing an estimate for thermal decomposition. The Supplementary Information discusses additional reactions and constants[50–55] and major uncertainties. The network includes 460 species and 3,406 forward reactions (W. Bains et al., manuscript in preparation).

We follow refs. [46,56] in temperature–pressure profiles from VIRA. Temperature–pressure profiles are from ref. [57], for the deep atmosphere profile (0–32 km) and for altitudes of 32–100 km (45° latitude profile adopted), while for altitudes of 100–112 km we use the VIRA dayside profile[58]. We followed refs. [46,56] in the Eddy diffusion profile, taken to be constant at $2.2 \times 10^3\,cm^2\,s^{-1}$ for altitude $z < 30$ km, $1 \times 10^4\,cm^2\,s^{-1}$ for 47–60 km, $1 \times 10^7\,cm^2\,s^{-1}$ for >100 km, and connected exponentially at intermediate altitudes. Extended Data Fig. 8 shows the temperature–pressure and Eddy diffusion profiles adopted in this work, along with decomposition timescales.

We take fixed[46] surface boundary conditions for the major atmospheric species, along with initial surface boundary conditions for minor species, radicals and atoms, except for PH_3. Observational constraints and initial surface model abundances are listed in Supplementary Tables 2 and 3. In validating our model, predictions for a variety of species compared with observations are plotted in Extended Data Fig. 9. Nearly all profiles agree with observations within an order of magnitude in concentration, within 5 km height; for full details, see Supplementary Information.

Extended Data Fig. 9 also summarizes wind data in relation to our observations of Venus. The latitudinal PH_3 variation is somewhat unexpected, implying that (1) the PH_3 observed is largely above 60 km and that this work and the models presented in this work and in refs. [46,48] correctly predict or under-predict the above-cloud concentrations of OH, H, O and Cl, or (2) that there is some unknown mechanism that more rapidly destroys PH_3 within the cloud layer, or both.

Potential pathways for PH_3 production. Potential PH_3-production pathways in the Venusian environment are discussed in detail in the Supplementary Information (W. Bains et al., manuscript in preparation; summarized in Extended Data Fig. 10). Two possible classes of routes for the production of PH_3 were considered: photochemical production or non-photochemical chemistry.

For photochemical modelling, we created a network of reactions of known kinetic parameters[59] that could lead from H_3PO_4 (phosphoric acid) to PH_3 (phosphine), by reaction with photochemically generated radicals in the Venusian atmosphere. Where reactions were possible but no kinetic data for the phosphorus species were known, homologous nitrogen species reaction kinetics were used instead, validated by comparing reactions of analogous nitrogen and phosphorus species. The maximum possible rate for reductive chemistry in this network was compared with the destruction rate as a function of altitude.

Non-photochemical reactions were modelled thermodynamically. For surface and atmospheric chemistry, we created a list of chemicals, their concentrations and reactions, for all potential PH_3 production reactions. Phosphorus species abundances were calculated themodynamically and assumed to be in equilibrium with liquid/solid species at the cloud base. The free energy of reaction, indicating whether the net production of PH_3 was thermodynamically favoured, was calculated using standard methods (see Supplementary Information for details). None of the reactions favour the formation of PH_3, on average having a free energy of reaction of $+100\,kJ\,mol^{-1}$ (Extended Data Fig. 7).

Modelling the subsurface chemistry was approached via oxygen fugacity (fO_2) (ref. [60]), the notional concentration of free oxygen in the crustal rocks. We model the equilibrium between phosphate and PH_3, for temperatures between 700 K and 1,800 K, at 100 or 1,000 bar, and with 0.01%, 0.2% and 5% water. Oxygen fugacity of plausible crust and mantle rocks based on Venus lander geological data is 8–15 orders of magnitude too high to support reduction of phosphate, so degassing of mantle rocks would produce only trivial amounts of PH_3. Volcanic, lightning and meteoritic delivery were calculated based on parallels with terrestrial rates of events within Venusian atmosphere, and were calculated to be negligible.

PH_3 and hypotheses on Venusian life. In the Supplementary Information, we briefly summarize ideas on why the temperate but hyperacidic Venusian clouds have been proposed for decades as potentially habitable, despite obvious difficulties such as resisting destruction by sulfuric acid. We earlier proposed that

any detectable PH_3 found in the atmosphere of a rocky planet is a promising sign of life[10] and showed that biological production of PH_3 is favoured by cool, acid conditions[18]. Initial modelling based on terrestrial biochemistry suggests that biochemical reduction of phosphate to PH_3 is thermodynamically feasible under Venus cloud conditions (W. Bains et al., manuscript in preparation). We have also described a possible life cycle for a Venusian aerial biosphere[61].

Data availability

The data that support the plots within this paper and other findings of this study are available from the corresponding author upon reasonable request. The raw data are publicly available at https://www.eaobservatory.org/jcmt/science/archive/ (JCMT) and http://almascience.eso.org/aq/ (ALMA). Source data are provided with this paper.

Code availability

Our reduction scripts that can be used with the raw data to reproduce the results shown are provided as Supplementary Software 1 (JCMT) and Supplementary Software 2–4 (ALMA).

Received: 7 February 2020; Accepted: 13 July 2020;
Published online: 14 September 2020

References

1. Baudino, J.-L. et al. Toward the analysis of JWST exoplanet spectra: identifying troublesome model parameters. *Astrophys. J.* **850**, 150 (2017).
2. Boston, P. J., Ivanov, M. V. & McKay, C. P. On the possibility of chemosynthetic ecosystems in subsurface habitats on Mars. *Icarus* **95**, 300–308 (1992).
3. McKay, C. P., Porco, C. C., Altheide, T., Davis, W. L. & Kral, T. A. The possible origin and persistence of life on Enceladus and detection of biomarkers in the plume. *Astrobiology* **8**, 909–919 (2008).
4. Pappalardo, R. T. et al. Does Europa have a subsurface ocean? Evaluation of the geological evidence. *J. Geophys. Res. Planets* **104**, 24015–24055 (1999).
5. Roth, L. et al. Transient water vapor at Europa's south pole. *Science* **343**, 171–174 (2014).
6. Waite, J. H. et al. Cassini Ion and Neutral Mass Spectrometer: Enceladus plume composition and structure. *Science* **311**, 1419–1422 (2006).
7. Postberg, F. et al. Macromolecular organic compounds from the depths of Enceladus. *Nature* **558**, 564–568 (2018).
8. Oehler, D. Z. & Etiope, G. Methane seepage on Mars: where to look and why. *Astrobiology* **17**, 1233–1264 (2017).
9. Gillen, E., Rimmer, P. B. & Catling, D. C. Statistical analysis of Curiosity data shows no evidence for a strong seasonal cycle of Martian methane. *Icarus* **336**, 113407 (2020).
10. Sousa-Silva, C. et al. Phosphine as a biosignature gas in exoplanet atmospheres. *Astrobiology* **20**, 235–268 (2020).
11. Pasek, M. A., Sampson, J. M. & Atlas, Z. Redox chemistry in the phosphorus biogeochemical cycle. *Proc. Natl. Acad. Sci. USA* **111**, 15468–15473 (2014).
12. Bregman, J. D., Lester, D. F. & Rank, D. M. Observation of the ν_2 band of PH_3 in the atmosphere of Saturn. *Astrophys. J.* **202**, L55–L56 (1975).
13. Tarrago, G. et al. Phosphine spectrum at 4–5 μm: analysis and line-by-line simulation of $2\nu_2$, $\nu_2 + \nu_4$, $2\nu_4$, ν_1, and ν_3 bands. *J. Mol. Spectrosc.* **154**, 30–42 (1992).
14. Noll, K. S. & Marley, M. S. in *Planets Beyond the Solar System and the Next Generation of Space Missions* (ed. Soderblom, D.) 155 (ASP, 1997).
15. Visscher, C., Lodders, K. & Fegley, B. Atmospheric chemistry in giant planets, brown dwarfs, and low-mass dwarf stars. II. Sulfur and phosphorus. *Astrophys. J.* **648**, 1181 (2006).
16. Morowitz, H. & Sagan, C. Life in the clouds of venus? *Nature* **215**, 1259 (1967).
17. Limaye, S. S. et al. Venus' spectral signatures and the potential for life in the clouds. *Astrobiology* **18**, 1181–1198 (2018).
18. Bains, W., Petkowski, J. J., Sousa-Silva, C. & Seager, S. New environmental model for thermodynamic ecology of biological phosphine production. *Sci.Total Environ.* **658**, 521–536 (2019).
19. Weisstein, E. W. & Serabyn, E. Detection of the 267 GHz $J = 1$-0 rotational transition of PH_3 in Saturn with a new Fourier transform spectrometer. *Icarus* **109**, 367–381 (1994).
20. Cram, T. A directable modular approach to data processing. *Astron. Astrophys. Suppl. Ser.* **15**, 339 (1974).
21. Warmels, R. et al. *ALMA Cycle 6 Technical Handbook* doc. 6.3 (ALMA, 2018).
22. Encrenaz, T., Moreno, R., Moullet, A., Lellouch, E. & Fouchet, T. Submillimeter mapping of mesospheric minor species on Venus with ALMA. *Planet. Space Sci.* **113**, 275–291 (2015).
23. Jacquinet-Husson, N. et al. The 2015 edition of the GEISA spectroscopic database. *J. Mol. Spectrosc.* **327**, 31–72 (2016).
24. Gordon, I. E. et al. The HITRAN2016 molecular spectroscopic database. *J. Quant. Spectrosc. Radiat. Transf.* **203**, 3–69 (2017).
25. Tennyson, J. et al. The ExoMol database: molecular line lists for exoplanet and other hot atmospheres. *J. Mol. Spectrosc.* **327**, 73–94 (2016).
26. Kuczkowski, R. L., Suenram, R. D. & Lovas, F. J. Microwave spectrum, structure, and dipole moment of sulfuric acid. *J. Am. Chem. Soc.* **103**, 2561–2566 (1981).
27. Piccialli, A. et al. Mapping the thermal structure and minor species of Venus mesosphere with ALMA submillimeter observations. *Astron. Astrophys.* **606**, A53 (2017).
28. Gurwell, M. A., Melnick, G. J., Tolls, V., Bergin, E. A. & Patten, B. M. SWAS observations of water vapor in the Venus mesosphere. *Icarus* **188**, 288–304 (2007).
29. Dartnell, L. R. et al. Constraints on a potential aerial biosphere on Venus: I. Cosmic rays. *Icarus* **257**, 396–405 (2015).
30. Sousa-Silva, C., Hesketh, N., Yurchenko, S. N., Hill, C. & Tennyson, J. High temperature partition functions and thermodynamic data for ammonia and phosphine. *J. Quant. Spectrosc.Radiat. Transf.* **142**, 66–74 (2014).
31. Sousa-Silva, C., Tennyson, J. & Yurchenko, S. N. Communication: tunnelling splitting in the phosphine molecule. *J. Chem. Phys.* **145**, 091102 (2016).
32. Krasnopolsky, V. A. Vega mission results and chemical composition of Venusian clouds. *Icarus* **80**, 202–210 (1989).
33. Lorenz, R. D. Lightning detection on Venus: a critical review. *Prog. Earth Planet. Sci.* **5**, 34 (2018).
34. Shalygin, E. V. et al. Active volcanism on Venus in the Ganiki Chasma rift zone. *Geophys. Res. Lett.* **42**, 4762–4769 (2015).
35. Grinspoon, D. H. & Bullock, M. A. in *Exploring Venus as a Terrestrial Planet* (eds Esposito, L. W., Stofan, E. R. & Cravens, T. E.) 191 (American Geophysical Union, 2007).
36. Sánchez-Lavega, A., Lebonnois, S., Imamura, T., Read, P. & Luz, D. The atmospheric dynamics of Venus. *Space Sci. Rev.* **212**, 1541–1616 (2017).
37. Currie, M. J. et al. Starlink Software in 2013. *Astron. Soc. Pac. Conf. Ser.* **485**, 391–394 (2014).
38. Currie, M. J. & Berry, D. S. KAPPA: Kernel Applications Package ascl:1403.022 (Astrophysics Source Code Library, 2014).
39. Jenness., T. et al. Automated reduction of sub-millimetre single-dish heterodyne data from the James Clerk Maxwell Telescope using ORAC-DR. *Mon. Not. R. Astron. Soc.* **453**, 73–88 (2015).
40. Škoda, P., Draper, P. W., Neves, M. C., Andrešič, D. & Jenness, T. Spectroscopic analysis in the virtual observatory environment with SPLAT-VO. *Astron. Comput.* **7**, 108–120 (2014).
41. Sandor, B. J. & Clancy, R. T. First measurements of ClO in the Venus atmosphere–altitude dependence and temporal variation. *Icarus* **313**, 15–24 (2018).
42. Barnes, D. G., Briggs, F. H. & Calabretta, M. R. Postcorrelation ripple removal and radio frequency interference rejection for Parkes Telescope survey data. *Radio Sci.* **40**, 1–10 (2005).
43. Butler, B. *ALMA Memo 594: Flux Density Models for Solar System Bodies in CASA* (ALMA Memo Series, NRAO, 2012).
44. Sandor, B. J. & Clancy, R. T. Water vapor variations in the Venus mesosphere from microwave spectra. *Icarus* **177**, 129–143 (2005).
45. Rimmer, P. B. & Helling, C. A chemical kinetics network for lightning and life in planetary atmospheres. *Astrophys. J. Suppl. Ser.* **224**, 9 (2016).
46. Krasnopolsky, V. A. Chemical kinetic model for the lower atmosphere of Venus. *Icarus* **191**, 25–37 (2007).
47. Rimmer, P. B. & Rugheimer, S. Hydrogen cyanide in nitrogen-rich atmospheres of rocky exoplanets. *Icarus* **329**, 124–131 (2019).
48. Krasnopolsky, V. A. S_3 and S_4 abundances and improved chemical kinetic model for the lower atmosphere of Venus. *Icarus* **225**, 570–580 (2013).
49. Zhang, X., Liang, M. C., Mills, F. P., Belyaev, D. A. & Yung, Y. L. Sulfur chemistry in the middle atmosphere of Venus. *Icarus* **217**, 714–739 (2012).
50. Burcat, A. & Ruscic, B. *Third Millenium Ideal Gas and Condensed Phase Thermochemical Database for Combustion (with Update from Active Th rmochemical Tables)* (Argonne National Laboratory, 2005).
51. Visscher, C. & Moses, J. I. Quenching of carbon monoxide and methane in the atmospheres of cool brown dwarfs and hot Jupiters. *Astrophys. J.* **738**, 72 (2011).
52. Lyons, J. R. An estimate of the equilibrium speciation of sulfur vapor over solid sulfur and implications for planetary atmospheres. *J. Sulphur Chem.* **29**, 269–279 (2008).
53. Kulmala, M. & Laaksonen, A. Binary nucleation of water–sulfuric acid system: comparison of classical theories with different H_2SO_4 saturation vapor pressures. *J. Chem. Phys.* **93**, 696–701 (1990).
54. Bierson, C. J. & Zhang, X. Chemical cycling in the Venusian atmosphere: a full photochemical model from the surface to 110 km. *J. Geophys. Res. Planets* https://doi.org/10.1029/2019JE006159 (2019).
55. Sander, R. Compilation of Henry's law constants (version 4.0) for water as solvent. *Atmos. Chem. Phys.* **15**, 4399–4981 (2015).

56. Krasnopolsky, V. A. A photochemical model for the Venus atmosphere at 47–112 km. *Icarus* **218**, 230–246 (2012).
57. Seiff, A. et al. Models of the structure of the atmosphere of Venus from the surface to 100 kilometers altitude. *Adv. Space Res.* **5**, 3–58 (1985).
58. Keating, G. M. et al. Models of Venus neutral upper atmosphere: structure and composition. *Adv. Space Res.* **5**, 117–171 (1985).
59. Linstrom, P. J. & Mallard, W. G. The NIST Chemistry WebBook: a chemical data resource on the internet. *J. Chem. Eng. Data* **46**, 1059–1063 (2001).
60. Frost, B. R. in *Oxide Minerals: Petrologic and Magnetic Significance* (ed. Lindsley, D. H.) Ch. 1 (Mineralogical Society of America, 1991).
61. Seager, S. et al. The Venusian lower atmosphere haze as a depot for desiccated microbial life: a proposed life cycle for persistence of the venusian aerial biosphere. *Astrobiology* https://doi.org/10.1089/ast.2020.2244 (2020).

Acknowledgements

Venus was observed under JCMT Service Program S16BP007 and ALMA Director's Discretionary Time programme 2018.A.00023.S. As JCMT users, we express our deep gratitude to the people of Hawaii for the use of a location on Mauna Kea, a sacred site. We thank M. Gurwell, I. Gordon and M. Knapp for useful discussions; personnel of the UK Starlink Project for training; S. Dougherty for award of ALMA Director's discretionary time; and D. Petry and other Astronomers on Duty and project preparation scientists at ALMA for ensuring timely observations. The James Clerk Maxwell Telescope is operated by the East Asian Observatory on behalf of The National Astronomical Observatory of Japan; Academia Sinica Institute of Astronomy and Astrophysics; the Korea Astronomy and Space Science Institute; Center for Astronomical Mega-Science (as well as the National Key R&D Program of China with no. 2017YFA0402700). Additional funding support is provided by the Science and Technology Facilities Council of the United Kingdom and participating universities in the United Kingdom (including Cardiff, Imperial College and the Open University) and Canada. Starlink software is currently supported by the East Asian Observatory. ALMA is a partnership of ESO (representing its member states), NSF (United States) and NINS (Japan), together with NRC (Canada), MOST and ASIAA (Taiwan), and KASI (Republic of Korea), in cooperation with the Republic of Chile. The Joint ALMA Observatory is operated by ESO, AUI/NRAO and NAOJ. Funding for the authors was provided by STFC (grant ST/N000838/1, D.L.C.); Radionet/MARCUs through ESO (J.S.G.); the Japan Society for the Promotion of Science KAKENHI (grant no. 16H02231, H.S.); the Heising-Simons Foundation, the Change Happens Foundation, the Simons Foundation (495062, S.R.); the Simons Foundation (SCOL award 59963, P.B.R.). RadioNet has received funding from the European Union's Horizon 2020 research and innovation programme under grant agreement no. 730562. J.S.G. is a Visitor at the Institute of Astronomy, University of Cambridge. S.R. is a SCOL Postdoctoral Fellow.

Author contributions

J.S.G. and A.M.S.R. analysed telescope data; H.S. developed a radiative transfer model; J.J.P. and W.B. worked out chemical kinetics and thermodynamics calculations; P.B.R., S.R., J.J.P., W.B. and S.S. worked on photochemistry; C.S.-S provided spectroscopic expertise and line parameter analysis; A.C., D.L.C., E.D.-M., H.J.F., C.S.-S., S.S., I.M.-W. and Z.Z. contributed expertise in astrochemistry, astrobiology, planetary science and coding; P.F., I.C., E.L. and J.H. designed, made and processed observations at the JCMT. J.S.G., A.M.S.R., W.B., J.J.P., D.L.C., S.S. and P.B.R. wrote the paper.

Competing interests

The authors declare no competing interests.

Additional information

Extended data is available for this paper at https://doi.org/10.1038/s41550-020-1174-4.

Supplementary information is available for this paper at https://doi.org/10.1038/s41550-020-1174-4.

Correspondence and requests for materials should be addressed to J.S.G.

Peer review information *Nature Astronomy* thanks Kevin Zahnle and the other, anonymous, reviewer(s) for their contribution to the peer review of this work.

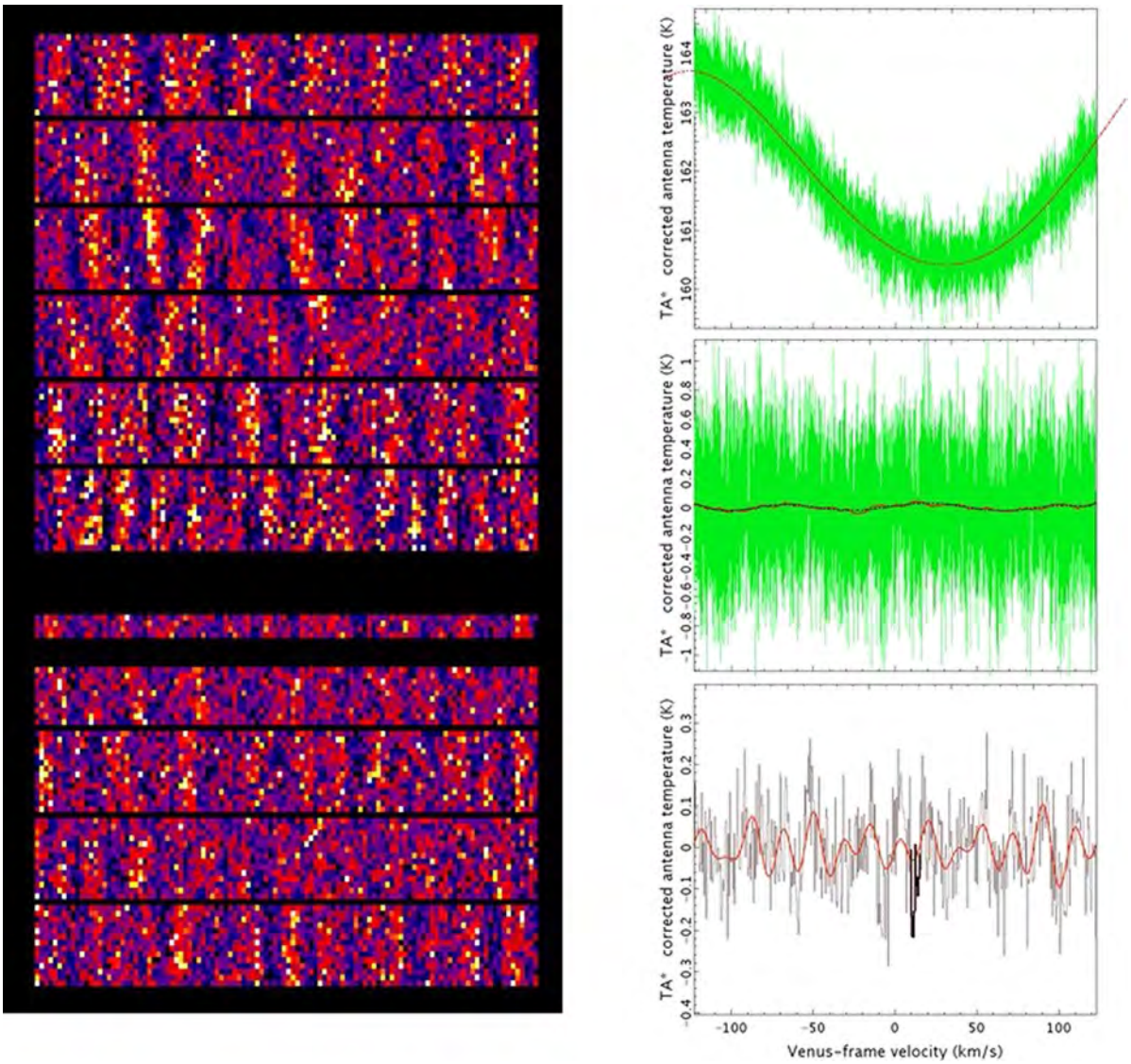

Extended Data Fig. 1 | Instrumental effects present in the JCMT data are illustrated. Data are shown after an initial step of blanking 512 channels with increasing noise towards each end of the 8192 channel passband. Left: the 140 sub-observations are stacked vertically, with spectral channel on the X-axis and time on the Y-axis (earliest observation at the bottom). The black bars every 15th row denote gaps between observations. Signatures of reflected signals have here been fitted and subtracted, leaving the ripples with ~8,16 periods across 250 MHz. The spectra have been binned to 2.2 km/s velocity resolution for clarity; the Doppler-shifted Venus absorption is then centered around channel 62 of 112, counting from the left. Right: stages of the reduction for observation 1 (bottom 14 rows of data in the left panel; note that this example is for demonstration, and script Data S1 in fact reduces every row in the left panel separately). Top-right panel shows the 4th-order polynomial fit (red dotted curve) to the full passband of observation 1. Middle-right panel shows the subsequent residual, overlaid with a median-filter (red curve) and the 9th-order fit to this filtered data (black dashed curve). Bottom-right panel shows the next subsequent residual, with the data binned to 0.55 km/s resolution (a section around Venus' velocity is highlighted with heavier bars). The overlaid red curve demonstrates the trend derived from the main Fourier components identified in the spectral ripple (via kappa task 'fourier').

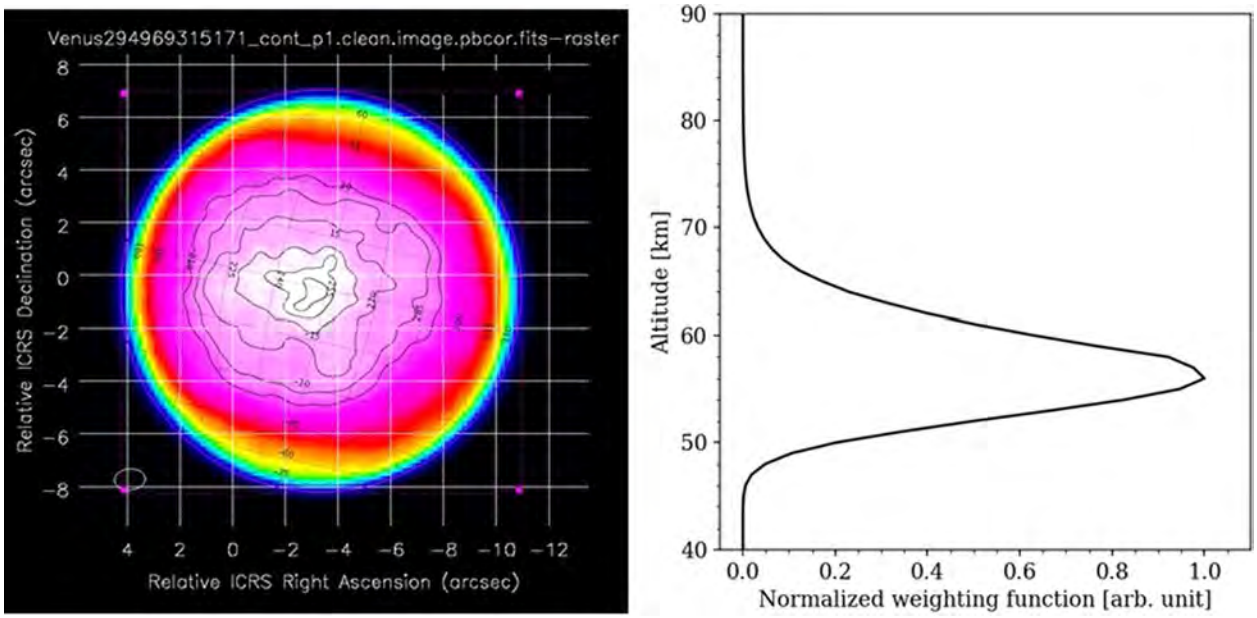

Extended Data Fig. 2 | Geometry of Venus is presented on the sky and by altitude. Left panel: Illustration of the orientation of Venus as viewed at the time of our ALMA observation. The sub-Earth point (center) is at longitude 256° and latitude -0.6°. The Sun was overhead at longitude 194° and latitude +0.2°, hence longitudes beyond the terminator (> 284°) were in darkness. (For comparison, during JCMT observations, the planet was just over half illuminated, with the sub-solar point closer to the left limb.) Planetary rotation is from right to left. The color scale shows the continuum signal in our observations, illustrating that the polar caps appear cooler. The overlaid contours were only used for checking alignment of the longitude/latitude grid, and do not show real structures (contour spacings are of order the noise of ~0.1 Jy/beam; this is higher than the spectral channel noise due to dynamic range limitations with all baselines included). Magenta outlines were also temporary guides. The ellipse at lower-left indicates the size and orientation of the ALMA beam for the continuum data (the beam for the line data is very similar). Right panel: Illustration of the altitude-range above which the phosphine absorption can originate. The weighting function shows the altitudes where the continuum (thermal) emission arises, at 266 GHz (near the PH_3 1-0 frequency but not affected by the absorption). The function peaks at 56 km and its FWHM spans approximately 53 to 61 km. The effect of uncertainties in the temperature profile of the Venusian atmosphere is to introduce systematics of order 2-3 km. The continuum emission has very high opacity, so our absorption observations do not trace altitudes below the peak of the weighting function.

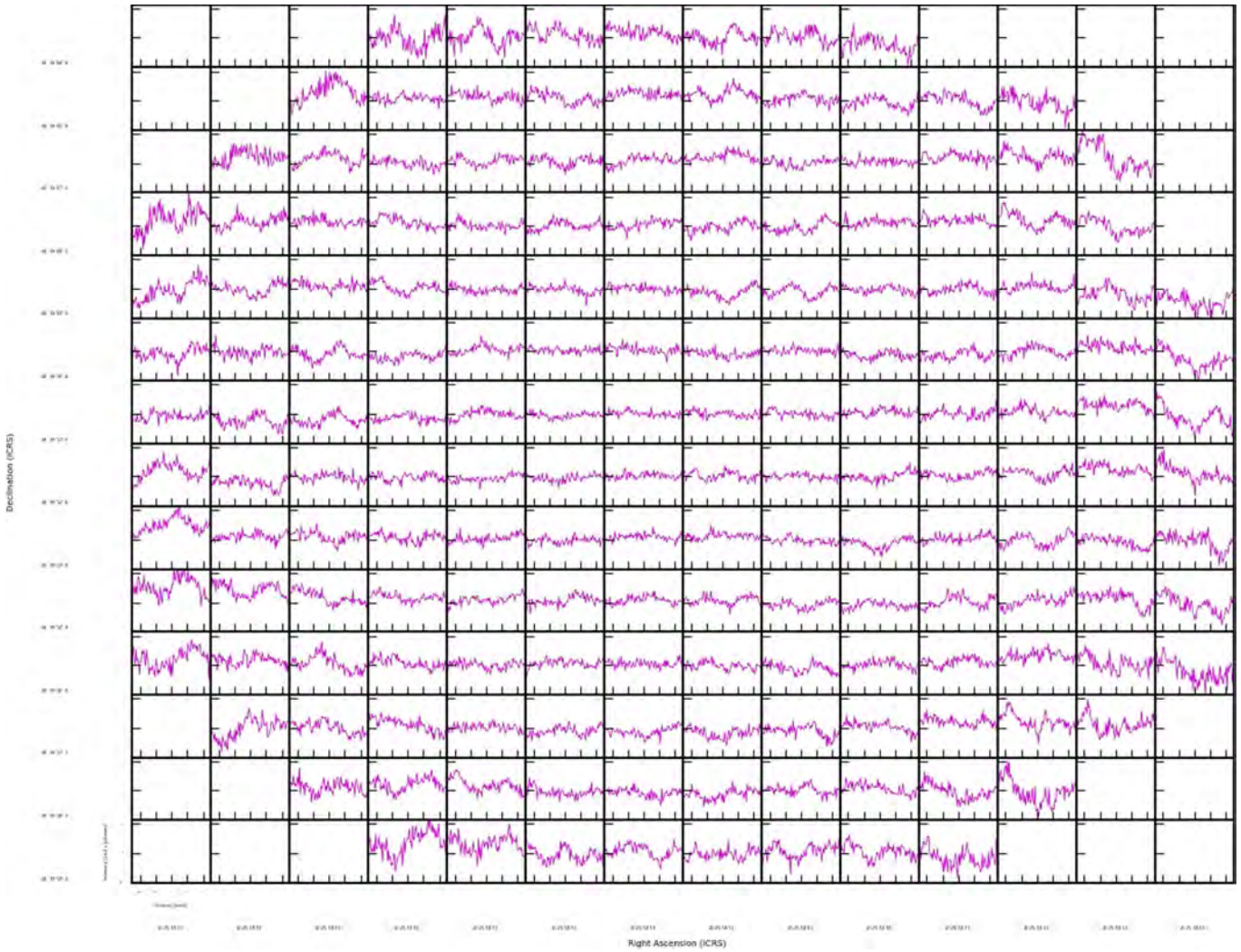

Extended Data Fig. 3 | Grid of PH_3 1-0 spectra from ALMA is presented, illustrating the difficulties of detecting the phosphine line on scales of the restoring beam. Each sub-plot spans 1.1 arcseconds on the planet (which has the same orientation as in Extended Data Fig. 2) and has an X-axis velocity range of ~ ±25 km/s. Blank boxes lie outside the planet (image mask has been applied).

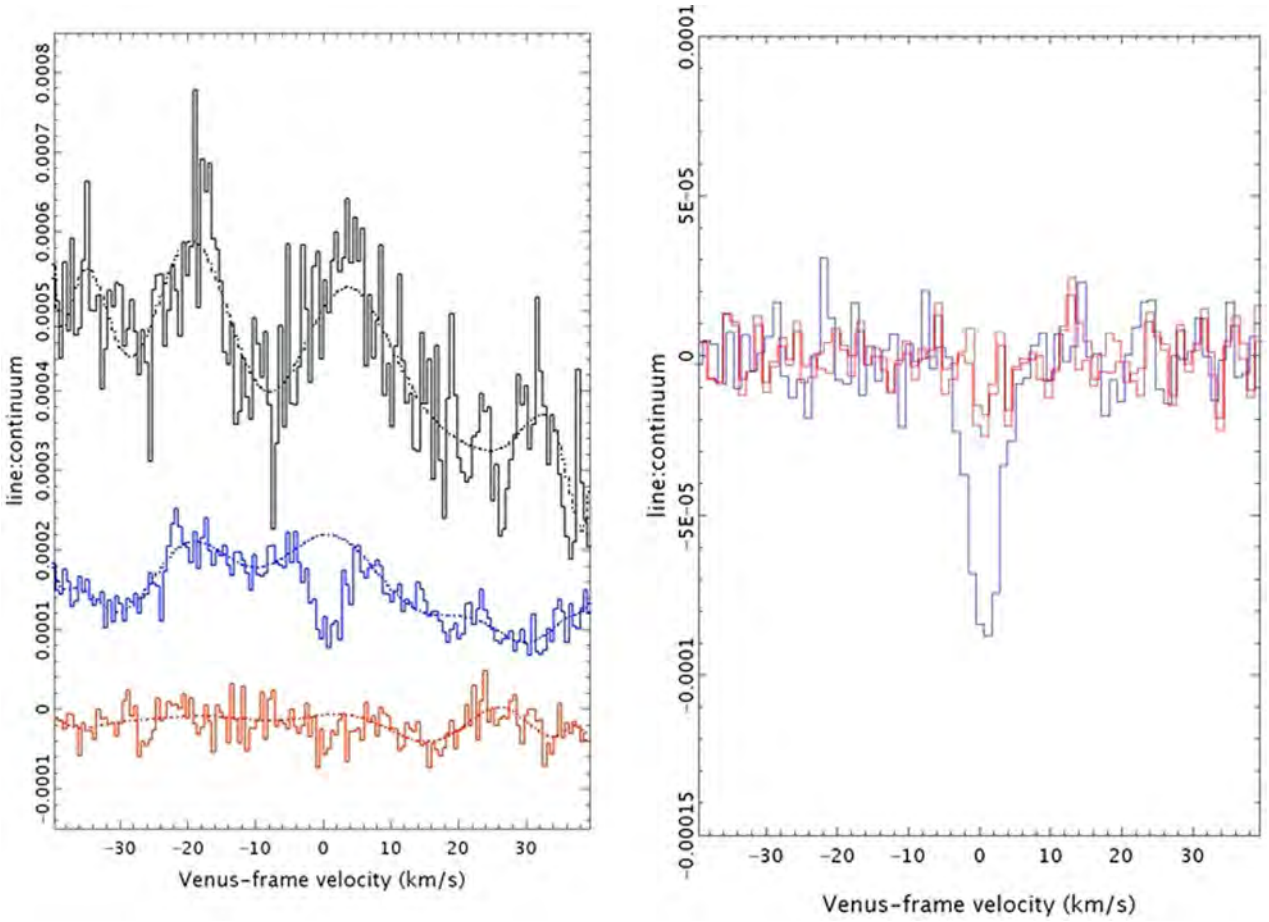

Extended Data Fig. 4 | Instrumental effects in the ALMA data are illustrated. Left panel: PH3 spectra (offset vertically for clarity) illustrating the 12th-order polynomial functions selected empirically for fitting the spectral ripple seen with ALMA (leading to the results of Fig. 2). The planetary zones are polar (top), mid-latitude (centre) and equatorial (bottom) as defined in Table 1. The complexity of the ripple drove the choice of $|v| = 5$ km/s, i.e. line wings more than 5 km/s from the velocity of Venus were forced to zero. This value of |v| was chosen from test-region spectra where the line was clearly visible, and then applied to all the latitudinal bands. The polar spectrum is more noisy because it includes a smaller area (Extended Data Fig. 2) and because ripple effects are larger at the planetary limb. Right panel: spectra (red histograms) produced for the whole planet after applying the same reduction procedures to regions of the passband offset by 400 spectral channels either side of the expected line location. This produces narrow artefacts spanning only ~2 spectral channels, much less broad than the real line (blue histogram). The l:c values (integrated over ±5 km/s) of the artefacts are 18 ± 4 % of the value for the real line.

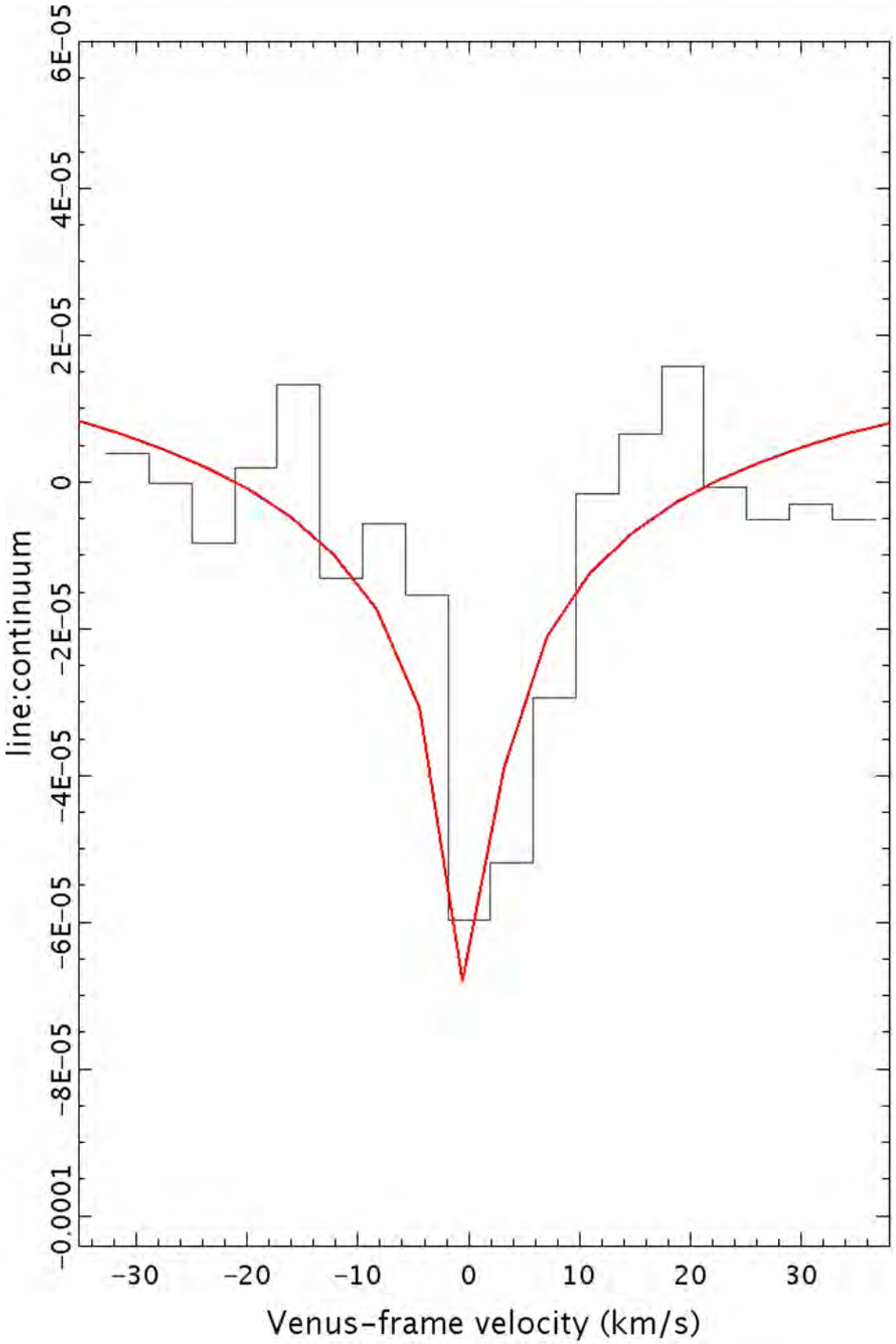

Extended Data Fig. 5 | Deuterated water (HDO) is detected on Venus in the ALMA data. A preliminary reduction of the whole-planet spectrum in the HDO $2_{2,0}$-$3_{1,3}$ transition is shown. The overlaid red curve is from our radiative transfer model, calculated for 2.5 ppb abundance and processed with a 1st-order polynomial fit, as for the data. No correction has been made for line-dilution, so the abundance can be significantly under-estimated, depending on the scale over which the molecules are distributed.

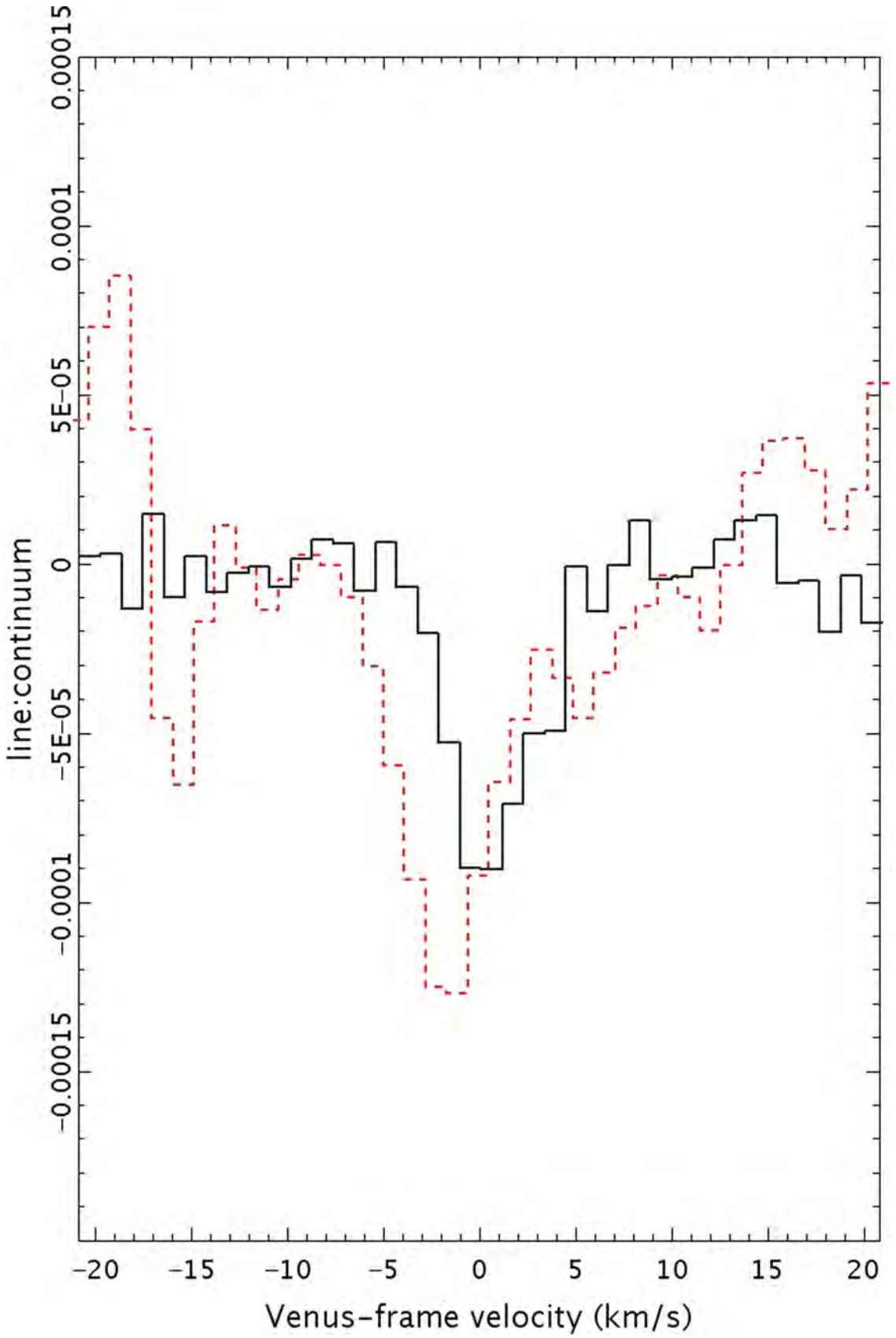

Extended Data Fig. 6 | The whole-planet PH_3 1-0 spectrum (black histogram) from narrowband ALMA data is superposed on the equivalent data recorded simultaneously in the wideband spectral configuration (red dashed histogram). The wideband spectrum has had a 1st-order polynomial subtracted to correct for mean level and overall slope. The narrowband spectrum (Fig. 2) is shown here at the 1.1 km/s resolution of the wideband data. The wideband absorption feature is substantially noisier due to a greater degree of spectral ripple (see e.g. the structure around -15 to -20 km/s), but it supports our PH_3 detection, i.e. this detection cannot be attributed to an artefact of one correlator configuration.

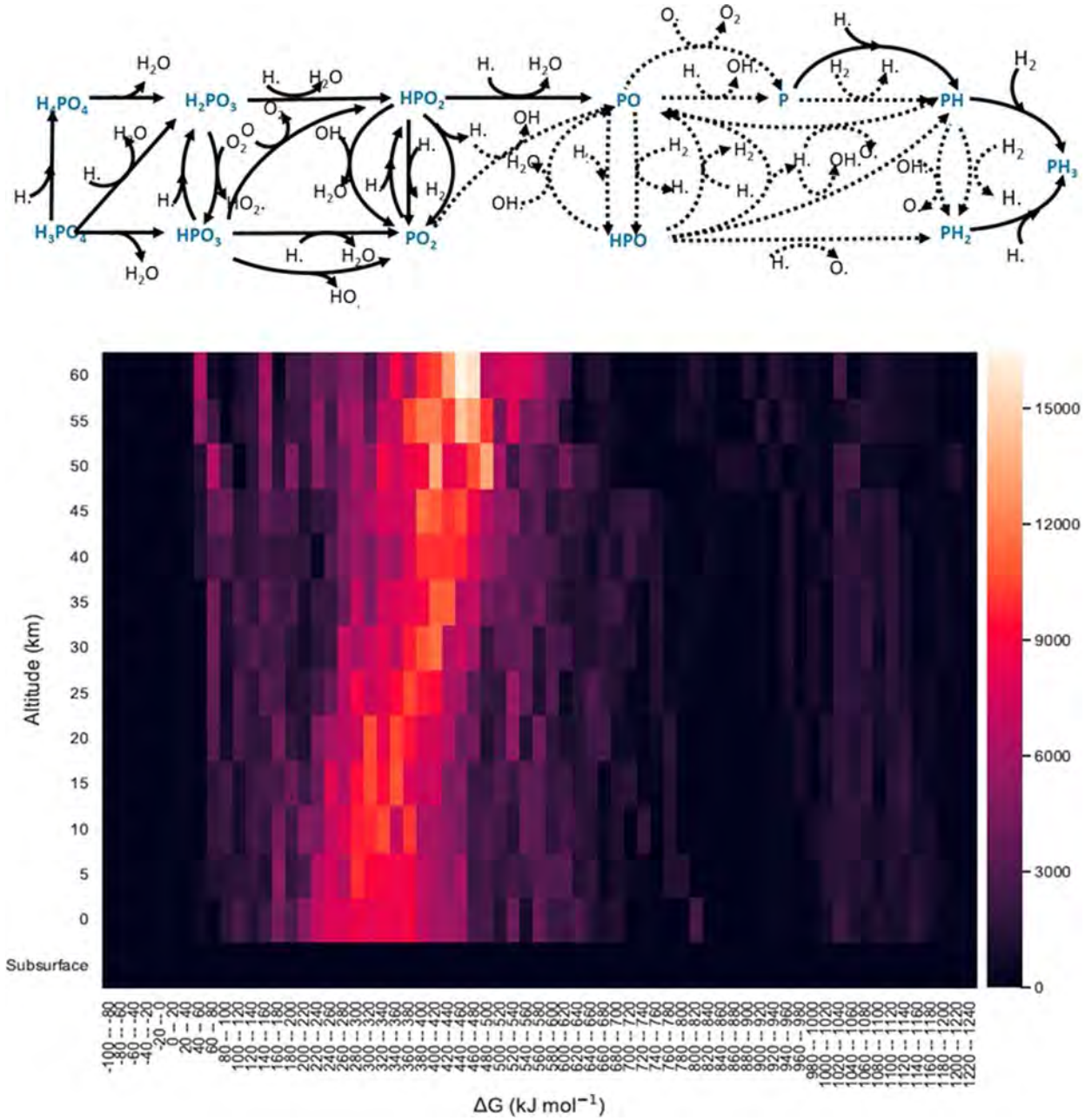

Extended Data Fig. 7 | Chemical pathways and energies are illustrated. Upper panel: Reaction network used to predict maximum possible photochemical production rate for phosphine. Continuous lines are reactions for which kinetic data for the phosphorus species is known. Dotted lines are reactions for which kinetic data for the analogous nitrogen species is known, and was used here. Phosphorus species are shown in blue, reacting radicals in black. Lower panel: Heat map showing that phosphine production is not thermodynamically favored. The plot shows how many reaction/condition combinations there are with given Gibbs free energy as a function of altitude. Y-axis is height above the surface (altitude, in km); columns are bins of data in X, the Gibbs Free Energy (ΔG: -100 to +1240 kJ mol^{-1}; 20 kJ mol^{-1} bins). Brighter-colored cells indicate more reactions for a given range of ΔG. There are no reactions occurring in the range where processes would be energetically favorable, i.e. there are no reactions/conditions where ΔG is negative and energy is released.

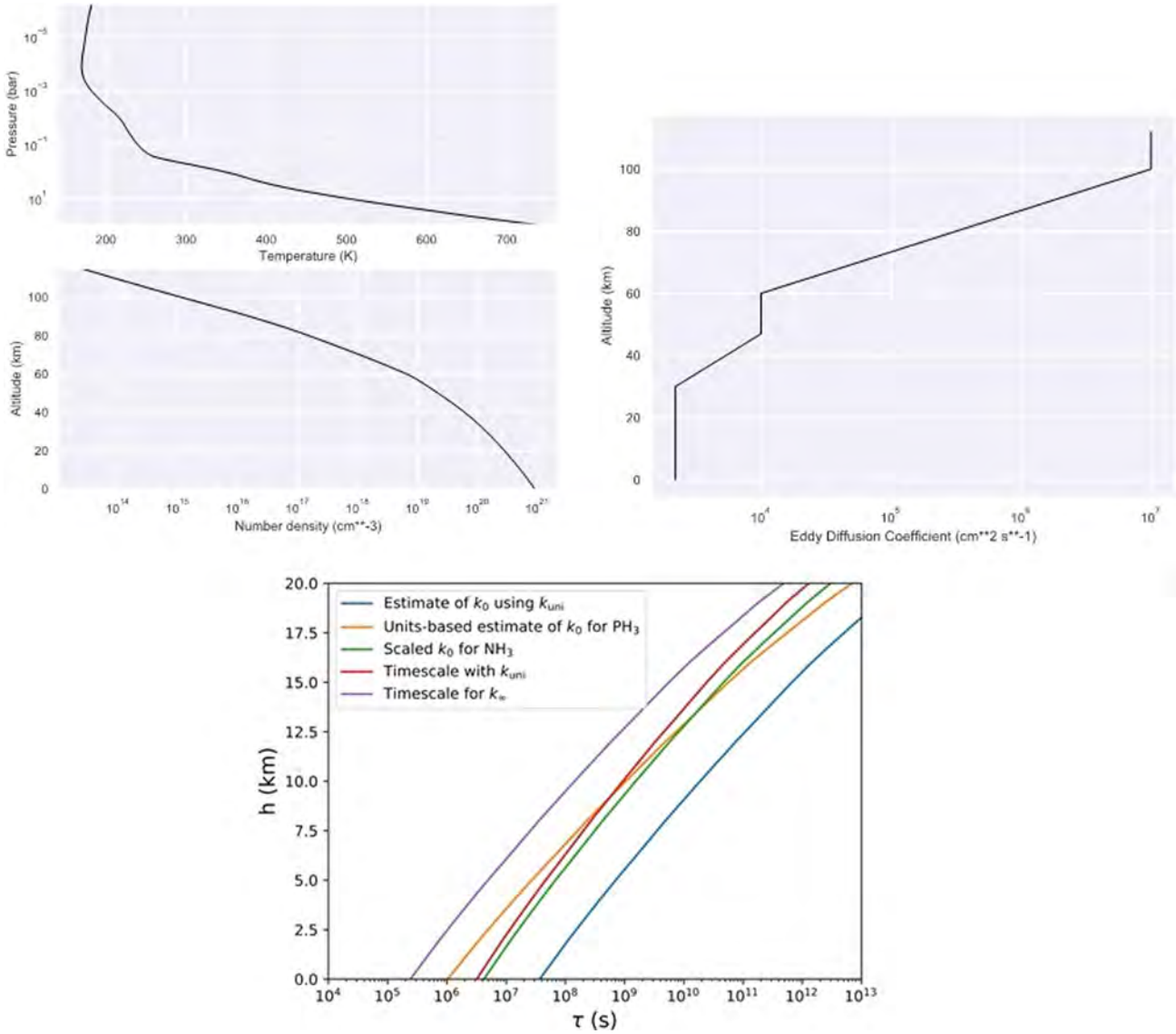

Extended Data Fig. 8 | Inputs to the photochemical modelling are illustrated. Top-left panel: Temperature-pressure profile used in photochemical modelling of the Venusian atmosphere, following refs. [46,56]. Top-right panel: Eddy diffusion profile used here in photochemical modelling of the Venusian atmosphere, following refs. [46,56]. Lower panel: Decomposition timescale for PH_3 as a function of height, derived from the Lindemann approximation of the rate constant, employing a theoretical value of k_∞ (s^{-1}) and an approximation of k_0 ($cm^3\ s^{-1}$) using k_{uni} (s^{-1}, blue), a simple unit-conversion estimate of k_0 (orange), a scaled estimate of k_0 based on ammonia decomposition (green), the timescale using only k_{uni} (red), and the timescale at the high pressure limit (violet).

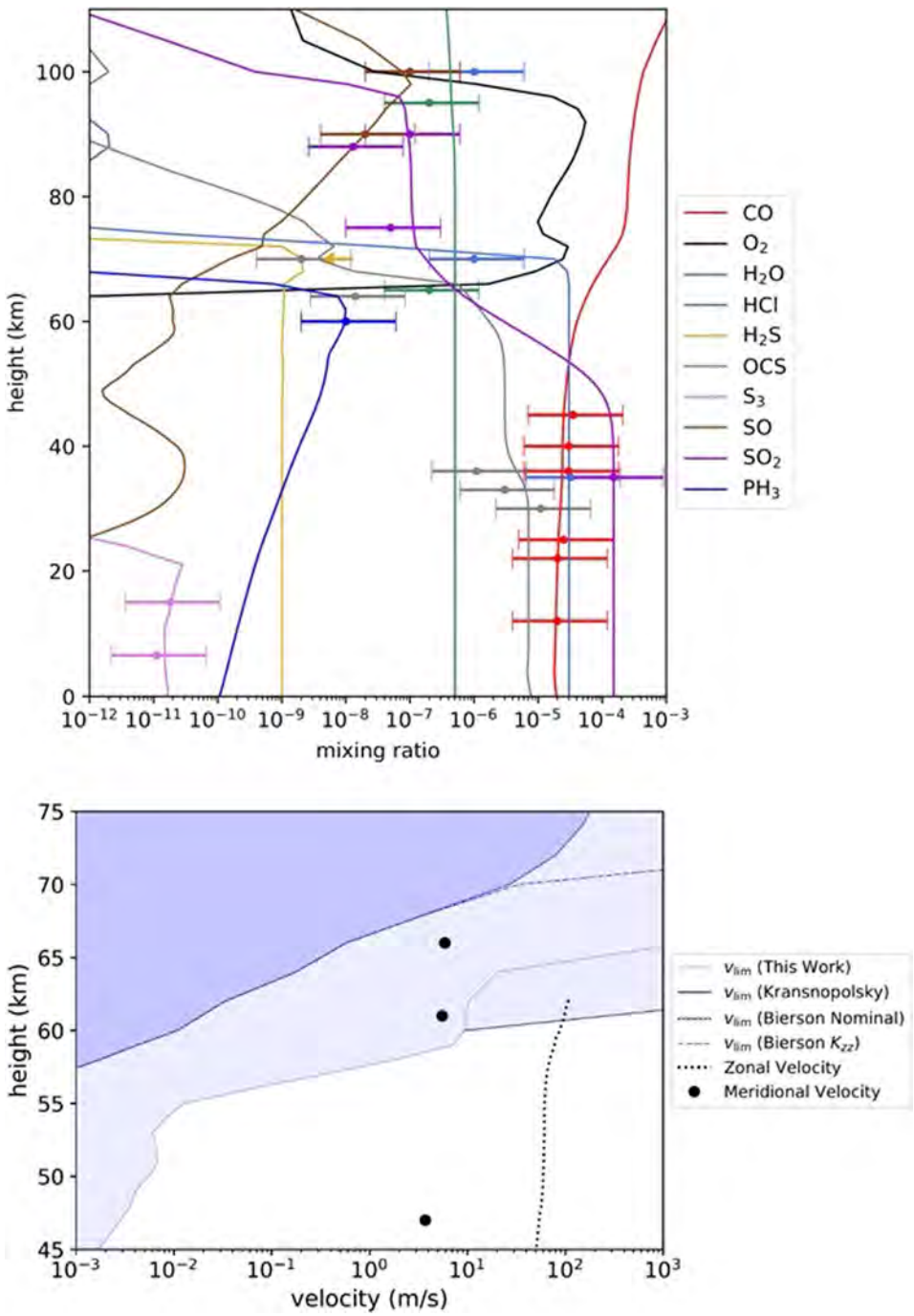

Extended Data Fig. 9 | Context of the photochemical modelling is illustrated. Top panel: Comparison of Venusian-atmosphere model to observations. Mixing ratios of various species are shown versus atmospheric height (km). Error bars span one order of magnitude, to help in comparing model predictions to observations. Bottom panel: Wind velocities that explain observed latitudinal variation, compared to observationally constrained zonal and meridional velocities. Velocities (m/s) are plotted versus atmospheric height (km). The blue shaded regions, bounded by blue lines, show the threshold velocities for the models in question. If the zonal wind velocity exceeds this threshold, then no longitudinal variation is expected, and if the meridional wind velocity exceeds this threshold, no latitudinal variation is expected. Estimated zonal[63] (dashed line) and meridional[64] (circles) wind velocities are also given.

Potential PH_3 Production Pathway on Venus	Quantitative Barriers for Production Pathway	Method
Equilibrium thermodynamics of chemical reactions between chemical species in the atmosphere and on the surface	Chemical reactions in Venusian environment are on average 100 kJ/mol too energetically costly (10 - 400 kJ/mol) to proceed spontaneously	Calculation of free energy from known or modeled gas concentrations
Equilibrium thermodynamics of chemical reactions in the subsurface	Oxygen fugacity of plausible crust and mantle rocks 8 - 15 orders of magnitude too high to support reduction of phosphate	Calculation of subsurface oxygen fugacity (fO_2)
Photochemical production by photochemically-generated reactive species	The required forward reaction rates are too low by factors of $10^4 - 10^5$	UV production of radicals followed by forward kinetic modelling from known and estimated reaction rates
Production by lightning	Limited frequency of lightning and low abundance of both atmospheric P species and reducing gases. Less than ppt of PH_3 is produced. PH_3 production is ~7 orders of magnitude too low to explain detected amounts	Calculations of the maximal efficiency of formation of PH_3 upon complete atomization of atmospheric and cloud components containing phosphorus. Literature review of lab experiments on the efficiency of formation of PH_3 by lightning discharges.
Meteoritic delivery as a source of phosphides and phosphine	The estimated maximal yearly meteoritic delivery of phosphine is ~8 orders of magnitude too low to explain detected amounts	Calculation of the maximum possible amounts of reduced P species delivered assuming their 100% conversion to PH_3
Large-scale comet/asteroid impact	Radar mapping of the surface of Venus shows no evidence of a recent large impact	
Other endergonic processes as potential sources of phosphine	Solar wind protons and large tribochemical processes cannot be responsible	

Extended Data Fig. 10 | An overview is presented of the potential pathways for phosphine production in the Venusian environment. None of the known processes can be responsible for the amount of phosphine detected in the Venusian atmosphere.